Radiation scattering in intense-field harmonic-generation experiments

C. de Lisio, C. Beneduce, R. Bruzzese, S. Solimeno, G. S. Sorrentino,
F. Vigilante, and C. Altucci

Dipartimento di Scienze Fisiche, Università di Napoli "Federico II," Mostra d'Oltremare Pad. 20, 80125 Napoli, Italy

Multiphoton ionization (MPI) of a noble gas produces an electron plasma, acting as a defocusing lens for the laser beam. In this paper we show that some parameters of the MPI process, e.g., order of nonlinearity p, and of the plasma, e.g., size and density, can be estimated by examining the far-field intensity distribution of the laser fundamental. In the limit of small electron density, describing the scattering within the framework of the Born approximation, an analytic expression of the scattered field has been obtained. For the other cases, we have developed a numerical approach based on the expansion of the field in a series of Gaussian beams. On the other hand, the aberration of the fundamental beam interferes notably with the process of harmonic generation in the gas medium. Our theoretical findings agree well with experimental data relative to the fundamental and the third harmonic of a Nd:YAG laser radiation (where YAG denotes yttrium aluminum garnet) produced in the nonresonant 14-photon ionization of Ar. This agreement confirms that the distributions reported in literature describe quite well the plasma formed in our 30-ps experiments.

I. INTRODUCTION

In harmonic-generation experiments carried out at intensities above 10^{13} W cm^{-2}, the effect of ionization becomes significant. The presence of free electrons introduces a space-time-dependent change of the refractive index of the medium. When the fraction of ionized atoms exceeds a few percent, the efficiency of harmonic generation is mainly dominated by the phase mismatch due to the electron plasma [1].

The medium ionization has been considered by Lago *et al.* [2], L'Huillier *et al.* [1, 3, 4], Lompré *et al.* [5], and Hutchinson *et al.* [6] by including in the phase-matching integral the contribution of the free electrons to the refractive index. At intensities of 10^{15}–10^{17} W cm^{-2} Auguste *et al.* [7] observed a strong defocusing of a laser beam focused in a cell filled with helium at relatively high pressure. Rae and Burnett [8] studied numerically the effects of the plasma formed in ultraintense ($I \gg 10^{15}$ W cm^{-2}) field interactions by using a one-dimensional model, which includes pulse propagation and ionization dynamics.

The aim of this paper is to analyze the effects of the plasma produced at intensities of the order of $I \approx 10^{12}$–10^{13} W cm^{-2} on both the incident beam and the harmonics. In a previous paper [9] we investigated the defocusing effect of the electron plasma on the harmonic beam in the weak field approximation by using the so-called complex eikonal formalism. Here we extend the previous analyis by following a complementary approach. In particular, we shall dwell on the scattering of the fundamental by the electron plasma formed in the focal region and on the pattern of the low-order harmonics.

We start from the low-density–low-intensity case, for which we shall derive an analytic representation of the scattered field, valid in the Born limit (single scattering). As a result of this analysis we will see that the structure of the pattern of the fundamental provides useful information about the transverse dimension w_{plasma} and the density of the plasma. In fact, the pattern consists of a central beam having the same geometrical parameters of the incident one and a sequence of scattered beams with beamwidths proportional to the square root of $p/2$, with p the order of the ionization process. By choosing adequate experimental conditions (atomic jet densities and laser intensities sufficiently small) it is possible to observe a pattern consisting only of a single scattered Gaussian beam with the incident beam superimposed. In these conditions it is possible to measure the ratio between the beamwidths of these two beams, so that the order p of the multiphoton ionization process can be estimated. The scattering process of the fundamental is well characterized by its scattering cross section σ: a measure of it provides useful information about the plasma geometry and the electron density. In fact, by measuring the fraction of power carried by the scattered beam the plasma density can be easily estimated.

Moreover, the harmonic field, e.g., the third harmonic, appears in the far field as a beam whose divergence is broader the larger the plasma density. We have analyzed several facets of the problem both experimentally and theoretically.

The above analysis, valid in the limit of single scattering, has been extended to the multiple-scattering case by integrating numerically the wave equations for the fundamental and the harmonics. To this end the fields have been expanded in a series of Gauss-Laguerre modes and the wave equations have been transformed in differential systems. Since the waist of the incident beam is much larger (4–5 times) than the plasma transverse dimension w_{plasma}, we have used Gaussian beams having spot size w intermediate between that of the incident beam w_0 and the plasma cross section w_{plasma}. In particular, accurate results can be achieved by assuming $w = w_0/2$.

The transport equations of the Gauss-Laguerre mode amplitudes $E_q^{(n)}$ have been put in simple forms by expanding the field in power series in the saturation parameter s (depending on the laser energy used in the ionization process) and in the phase $\Delta\phi$ (measuring the effective dephasing undergone by the incident beam in passing through the plasma). As a result of several computations we found that for $\Delta\phi \leq 10$ the patterns and the mode amplitudes are well approximated by expressions truncated at first order in $\Delta\phi$.

The scattering of the fundamental beam by the electron plasma in the framework of the Born approximation is described in Sec. II, while in Sec. III we illustrate a numerical method for integrating the wave equation for the fundamental field by expanding it in a superposition of TEM_{m0} Gaussian modes. The coefficients $E_1^{(m)}$ of this expansion form a vector $\mathbf{E}_1$, which is a function of the longitudinal coordinate. Section IV is dedicated to the the harmonic beam, which is represented as a combination of Gauss-Laguerre modes $u_q^{(r)}$ weighted by coefficients $E_q^{(r)}$. The far-field components $E_{q(\text{out})}^{(r)}$ play the role of partial phase-matching integrals, analogous to the phase-matching integral used in Ref. [1]. The experimental setup is illustrated in Sec. V, while in Sec. VI experimental data are presented and compared with the results of numerical simulation based on the Gaussian beam expansion. Finally, a discussion of the results and the limits of the present approach are presented in Sec. VII. The matrices occurring in the modal analysis of the fundamental beam are discussed in Appendix A, while the extension of the Gaussian beam expansion to the harmonics is presented in Appendix B. An integral expression of the mode amplitudes is derived in Appendix C. In Appendix D the harmonic mode amplitudes are derived in the limit of small electron density. The beam divergence is analyzed in Appendix E.

II. PROPAGATION OF THE FUNDAMENTAL BEAM

Let us consider a well collimated pulsed beam of frequency ω_1 ($k_1 = \omega_1/c$) propagating along the z axis,

$$E_1(\mathbf{r}, t) = e^{ik_1 z - i\omega_1 t}\mathcal{E}_1(\mathbf{r}, t), \tag{1}$$

inducing a polarization in an atomic jet,

$$P_1(\mathbf{r}, t) = e^{ik_1 z - i\omega_1 t}\mathcal{P}_1(\mathbf{r}, t)$$
$$\equiv \epsilon_0 e^{ik_1 z - i\omega_1 t}\left[\nu_1^2(\mathbf{r}, t) - 1\right]\mathcal{E}_1(\mathbf{r}, t) \tag{2}$$

with $\nu_1(\mathbf{r}, t)$ a space-time-depependent refractive index. For plasmas produced in harmonic-generation experiments, $\Delta\nu_1 \equiv \nu_1 - 1$ is generally so small that $\nu_1^2 - 1$ can be replaced by $2\Delta\nu_1$, while the envelope $\mathcal{E}_1$ satisfies the paraxial wave equation

$$\left[\nabla_t^2 + 2ik_1\left(\frac{\partial}{\partial z} + \frac{1}{c}\frac{\partial}{\partial t}\nu_1^2\right) + 2k_1^2\Delta\nu_1\right]\mathcal{E}_1 = 0. \tag{3}$$

The index 1 has been introduced in order to distinguish the quantities relative to the fundamental from the qth harmonic ones.

Now, we introduce the coordinate system $t^* = t - z/c, z, \mathbf{r}_t$ and express the incident beam $\mathcal{E}_{\text{in}}$ (not perturbed by the atomic beam) and $\mathcal{E}_1$ in the form

$$\mathcal{E}_{\text{in}}(\mathbf{r}, t) = \sqrt{I_1}\theta(t^*)u_{\text{in}}(\mathbf{r}),$$
$$\mathcal{E}_1(\mathbf{r}, t) = \sqrt{I_1}\theta(t^*)u_1(\mathbf{r}, t^*), \tag{4}$$

where I and $\theta(t^*)$ stand, respectively, for the peak power and the pulse profile of the incident beam. In particular $\lim_{z \to -\infty} u_1(\mathbf{r}, t^*) = u_{\text{in}}(\mathbf{r})$. Plugging the right-hand side of (4.b) into (3) yields

$$\left[\nabla_t^2 + 2ik_1\left(\frac{2}{c}\frac{\partial}{\partial t^*}\Delta\nu_1 + \frac{\partial}{\partial z}\right) + 2k_1^2\Delta\nu_1\right]u_1 = 0. \tag{5}$$

When we consider pulses longer than some hundred periods and with intensities such that $\Delta\nu_1$ is much smaller than unity we can drop the time derivative from Eq. (5) by recalling that the partial derivative with respect to z is calculated by keeping constant the retarded time t^*.

If we represent u_1 as a product of the incident beam u_{in} [$u_{\text{in}}(\mathbf{0}, t) = 1$] times a factor $e^{ik_1 S}$

$$u_1 = e^{ik_1 S}u_{\text{in}} \tag{6}$$

with S the so-called aberration eikonal (see, e.g., [9]), using the property of u_{in} of being an integral of (5) for $\Delta\nu_1 = 0$, we obtain

$$-\nabla_t S \cdot \nabla_t S + ik_1^{-1}\nabla_t^2 S$$

$$+ik_1^{-1}\nabla_t S \cdot \nabla_t \ln(u_{\text{in}}) - 2\frac{\partial S}{\partial z} + 2\Delta\nu_1 = 0. \tag{7}$$

Finally, ignoring the terms with the factor k_1^{-1} in front and considering an incident beam and a particle number distribution rotationally invariant around the propagation axis, Eq. (7) reduces to the eikonal equation

$$\frac{1}{2}\left(\frac{\partial S}{\partial \rho}\right)^2 + \frac{\partial S}{\partial z} = \Delta\nu_1, \tag{8}$$

ρ being the transverse coordinate. Lago *et al.* [2] and L'Huillier *et al.* [1] have neglected the terms proportional to the transverse gradient and have set $S = \int \Delta\nu_1 dz$.

When the beam u_{in} is strongly focused, the term in Eq. (7) proportional to the transverse gradient of $\ln(u_{\text{in}})$ cannot be neglected. In fact, for a TEM_{00} Gaussian beam

$$u_{\text{in}}(\rho, z) = \frac{1}{1 + iz/b}\exp\left[-\frac{k_1\rho^2}{2(b + iz)}\right] \tag{9}$$

we have $\nabla_t \ln u_{\text{in}} = -k_1\rho/(b + iz)$ and Eq. (8) must be rewritten as

$$\frac{1}{2}\left(\frac{\partial S}{\partial \rho}\right)^2 + \frac{\rho}{b + iz}\frac{\partial S}{\partial \rho} + \frac{\partial S}{\partial z} = \Delta\nu_1. \tag{10}$$

Inserting now the approximate expression of $S = \int \Delta\nu_1 dz$ in Eq. (10) we see that it can be used only when

$$\frac{\rho}{b}\left|\frac{\partial \int \Delta\nu_1 dz}{\partial \rho}\right| \ll |\Delta\nu_1|. \tag{11}$$

If we indicate by w_{plasma} and l_{plasma} the transverse and longitudinal dimensions of the electron plasma present in the focal region, the above inequality can be recast as

$$\frac{w_0}{b} \ll \frac{w_{plasma}}{l_{plasma}}, \tag{12}$$

with w_0 the radius of the laser spot at the waist. This condition is satisfied only when the extension of the atomic jet is much shorter than the confocal parameter b. In the other cases $w_0/w_{plasma} \approx \sqrt{p}$ and $l_{plasma}/b \approx \sqrt{\ln 2}/\sqrt{p}$ (p being the order of nonlinearity) and the two sides of (12) are almost equal.

The limitations imposed by Eq. (12) can be partially removed for $\Delta\nu_1$ very small by representing u_1 as the superposition of u_{in} and the field u_{sc} scattered by the partially ionized medium,

$$u_1(\mathbf{r}, t^*) = u_{sc}(\mathbf{r}, t^*) + u_{in}(\mathbf{r}) \tag{13}$$

where

$$u_{sc}(\mathbf{r}, t^*) = k_1^2 \int_{-\infty}^{z} dz' \int\int_{-\infty}^{\infty} d\mathbf{r}'_t G_F(\mathbf{r}_t, \mathbf{r}'_t; |z - z'|)$$
$$\times \Delta\nu_1(\mathbf{r}'_t, z'; t^*) u_1(\mathbf{r}'_t, z'; t^*), \tag{14}$$

G_F being the free-space Green's function in the paraxial (Fresnel) approximation [see Ref. [10], Eq. (3.07)]. When the leading-phase

$$\phi = k_1 \int_{-\infty}^{\infty} \Delta\nu_1 dz \tag{15}$$

of the incident beam along the plasma z axis is sufficiently small (namely, $\phi \ll 1$), the scattered field becomes negligible with respect to the incident one and u_1 can be replaced by u_{in} in the above integral (Born approximation),

$$u_{sc}(\mathbf{r}, t^*) = 2k_1^2 \int_{-\infty}^{z} dz' \int\int_{-\infty}^{\infty} d\mathbf{r}'_t G_F(\mathbf{r}_t, \mathbf{r}'_t; |z - z'|)$$
$$\times \Delta\nu_1(\mathbf{r}'_t, z'; t^*) u_{in}(\mathbf{r}'_t, z'). \tag{16}$$

For ionized gases the refractive index depends on the plasma frequency. At $\lambda = 1.06$ μm,

$$\Delta\nu_1 = -0.5 \times 10^{-21} \mathcal{N}_e, \tag{17}$$

with $\mathcal{N}_e$ the electron number density expressed in cm^{-3}.

When the ionization depends on a power of order p of the laser intensity [1, 11, 12] the electron density $\mathcal{N}_e$ can be expressed as

$$\mathcal{N}_e(z, \rho; t^*) = \mathcal{N}(z)\left[1 - \exp(-P_i)\right] = \mathcal{N}_{max} f(z, \rho; t^*), \tag{18}$$

where P_i represents the ionization probability and $\mathcal{N}(z)$ the distribution of neutral atoms along z. For a nonresonant p-photon ionization process characterized by a cross section $\sigma^{(p)}$, P_i is given by

$$P_i = s(t^*) \frac{\int_{-\infty}^{t^*} \theta^{2p}(t')|u_1|^{2p} dt'}{\int_{-\infty}^{t^*} \theta^{2p}(t') dt'}$$
$$\equiv s_{max} \int_{-\infty}^{t^*} \theta^{2p}(t')|u_1|^{2p} dt', \tag{19}$$

with $s(t^*) = \sigma^{(p)}(I/\hbar\omega)^p \int_{-\infty}^{t^*} \theta^{2p}(t') dt' = s_{max} \int_{-\infty}^{t^*} \theta^{2p}(t') dt' / \int_{-\infty}^{\infty} \theta^{2p}(t') dt'$ the saturation parameter for the pth-order multiphoton ionization process.

In the following we will express the plasma refractive index deviation by means of the function $f(\mathbf{r}; t^*) \leq 1$ defined in Eq. (18),

$$\Delta\nu_1 = -\Delta\nu_{max} f, \tag{20}$$

with $\Delta\nu_{max} = 0.5 \times 10^{-21} \mathcal{N}_{max}$. In the numerical simulations discussed in the following, we have assumed a sech^2 profile for the laser pulse intensity $\theta(t^*) = \mathrm{sech}(1.76t^*/\tau)$, with τ the laser pulse duration, and we have set $s(t^*) = s_{max} \int_{-\infty}^{t^*} \cosh^{-2p}(1.76t'/\tau) dt' / \int_{-\infty}^{\infty} \cosh^{-2p}(1.76t'/\tau) dt'$. In particular, for an ionization process with $p = 14$ (Ar ionization at $\lambda = 1.06$ μm) $\int_{-\infty}^{\infty} \cosh^{-2p}(1.76t'/\tau) dt' = 0.27\tau$.

For discussing the field scattered in the Born limit, it is worth expressing $\Delta\nu_1$ and u_{sc} as power series in the saturation parameter

$$\Delta\nu_1 = -\Delta\nu_{max} \sum_{k=1}^{\infty} \frac{(-s)^k}{k!} \nu^{(k)},$$
$$u_{sc} = -\Delta\nu_{max} \sum_{k=1}^{\infty} \frac{(-s)^k}{k!} u_{sc}^{(k)}, \tag{21}$$

with

$$\nu^{(k)} = \frac{\mathcal{N}(z)}{\mathcal{N}_{max}} |u_{in}|^{2pk},$$
$$u_{sc}^{(k)}(\rho, z) = 2k_1^2 \int_{-\infty}^{z} dz' \int\int_{-\infty}^{\infty} d\mathbf{r}'_t G_F(\mathbf{r}_t, \mathbf{r}'_t; |z - z'|)$$
$$\times \nu^{(k)}(\mathbf{r}'_t, z') u_{in}(\mathbf{r}'_t, z'). \tag{22}$$

For an incident field u_{in} having the form of a TEM$_{00}$ Gaussian beam [see Eq. (9)], the leading phase ϕ will be equal to [see Eqs. (15) and (20)]

$$\phi(t^*) = \Delta\phi \overline{f}(t^*), \tag{23}$$

with $\Delta\phi = k_1 b \Delta\nu_{max} = 0.5 \times 10^{-21} k_1 b \mathcal{N}_{max}$ and $\overline{f} = \int_{-\infty}^{\infty} f(z, 0; t^*) dz/b$. The latter quantity is plotted in Fig. 1 as a function of the saturation parameter. In typical experiments the confocal parameter b is of the order of 1–5 mm and $k_1 b$ is about 1–5 $\times$ 10^4, so that $\Delta\phi \approx 10^{-17} \mathcal{N}_{max}$. Since $\overline{f}$ is less than one for $s \leq 6$, the Born approximation holds true for plasmas having number particle densities smaller than 10^{17} cm^{-3}.

Now in order to evaluate the integral (22) it is worth noting that the product $\nu^{(k)} u_{in}$ is proportional to the complex amplitude $a^{(k)}$ of a Gaussian beam

$$\nu^{(k)}(\rho, z) u_{in}(\rho, z) = \frac{\mathcal{N}}{\mathcal{N}_{max}} |u_{in}|^{2pk} u_{in}$$
$$\equiv \frac{\mathcal{N}}{\mathcal{N}_{max}} c^{(k)}(z) a^{(k)}(\rho, z), \tag{24}$$

where

$$a^{(k)} = \frac{1}{1 + iz^{(k)}/b^{(k)}} \exp\left[-\frac{k_1\rho^2}{2(b^{(k)} + iz^{(k)})}\right],$$

$$c^{(k)} = \frac{1}{(1 + z^2/b^2)^{pk}} \frac{1 + iz^{(k)}/b^{(k)}}{1 + iz/b}, \qquad (25)$$

with

$$\frac{1}{b^{(k)} + iz^{(k)}} \equiv \frac{1}{b + iz} + \frac{2kpb}{b^2 + z^2}. \qquad (26)$$

$a^{(k)}(\rho, z)$ represents the amplitude at the point (ρ, z) of a Gaussian beam of confocal parameter $b^{(k)}$ and waist in $\zeta^{(k)} = z - z^{(k)}$. On the other hand, the diffraction

integral $-2ik_1 \int \int_{-\infty}^{\infty} G_F a d\mathbf{r}'$ transforms a Gaussian distribution having the form of $a^{(k)}(\mathbf{r}_t, z)$ into a Gaussian beam $a^{(k)}(\mathbf{r}'_t, z')$. Accordingly, the integral (22) relative to a thin region extending from z to $z + dz$ is equal to

$$du_{sc}^{(k)}(\rho', z'; z)$$

$$= ik_1 dz \; c^{(k)}(z) \frac{\mathcal{N}(z)}{\mathcal{N}_{\max}} \frac{1}{1 + i(z' - z + z^{(k)})/b^{(k)}}$$

$$\times \exp\left\{-\frac{k_1\rho'^2}{2\left[b^{(k)} + i(z' - z + z^{(k)})\right]}\right\}. \qquad (27)$$

Then summing over z gives the total scattered field

$$u_{sc}^{(k)}(\rho', z') = ik_1 \int_{-\infty}^{z'} \frac{\mathcal{N}(z)}{\mathcal{N}_{\max}} c^{(k)}(z) \frac{1}{1 + i(z' - z + z^{(k)})/b^{(k)}} \times \exp\left\{-\frac{k_1\rho'^2}{2\left[b^{(k)} + i(z' - z + z^{(k)})\right]}\right\} dz$$

$$\xrightarrow[z' \to \infty]{} \frac{k_1 b^2}{z'} C^{(k)} \exp\left(-\frac{k_1 b \rho'^2}{4kpz'^2} + i\frac{k_1\rho'^2}{2z}\right), \qquad (28)$$

where

$$C^{(k)} = \frac{1}{b^2} \int_{-\infty}^{\infty} \frac{\mathcal{N}(z)}{\mathcal{N}_{\max}} c^{(k)}(z) b^{(k)}(z)$$

$$\times \exp\left[-\frac{k_1\rho'^2}{2z'^2}\left(b^{(k)} - \frac{b}{2kp}\right)\right] dz. \qquad (29)$$

Setting $z = b\tan\psi$, $z^{(k)} = b^{(k)}\tan\psi^{(k)}$, and using Eq. (26) yields

$$\frac{b^{(k)}}{b} = \frac{1 + 2kp}{|1 + 2kpe^{i\psi}\cos\psi|^2},$$

$$\frac{b^{(k)}}{b}c^{(k)} = \frac{\cos^{2kp}\psi}{1 + 2kpe^{i\psi}\cos\psi}. \qquad (30)$$
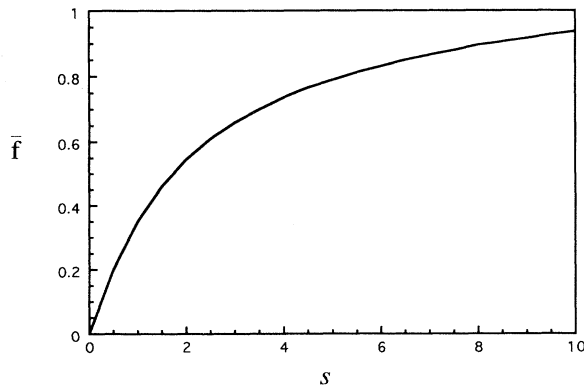
For large values of kp and $k_1 b$, Eq. (29) reduces to

FIG. 1. $\bar{f}$ versus the saturation parameter s for a TEM$_{00}$ Gaussian beam [see Eq. (23)].

$$C^{(k)} \approx \frac{1}{2kp} \int_{-\pi/2}^{\pi/2} \frac{\mathcal{N}(\psi)}{\mathcal{N}_{\max}} e^{-i\psi} \cos^{2kp-3}\psi d\psi. \qquad (31)$$

In particular, for a symmetric particle number distribution represented by the series

$$\frac{\mathcal{N}(\psi)}{\mathcal{N}_{\max}} = \sum_{l=0}^{\infty} N_l \cos^{2l}\psi, \qquad (32)$$

using the relation (see [13], integral No. 3.631.17)

$$\cos^{2m} x = \sum_{n=-m}^{m} c(m, n)e^{i2nx} \qquad (33)$$

with

$$c(m, n) = \frac{1}{2^{2m}}\binom{2m}{m + |n|}, \qquad (34)$$

$C^{(k)}$ can be expressed as

$$C^{(k)} \approx \frac{1}{kp} \sum_{l} N_l c(kp + l - 1, 0). \qquad (35)$$

In conclusion, in the Born limit the field u_1 is a superposition of TEM$_{00}$ Gaussian beams with different confocal parameters

$$u_1(\mathbf{r}; t^*) \propto \exp\left(-\frac{k_1 b}{2}\frac{\rho^2}{z^2}\right)$$

$$+ i\Delta\phi \sum_{k=1}^{\infty} \frac{[-s(t^*)]^k}{k!} C^{(k)} \exp\left(-\frac{k_1 b}{4kp}\frac{\rho^2}{z^2}\right), \qquad (36)$$

with $\Delta\phi$ defined in (23). Accordingly, the incident power is scattered in a sequence of Gaussian beams with divergences equal to $\sqrt{2kp}$ times the divergence of the inci-
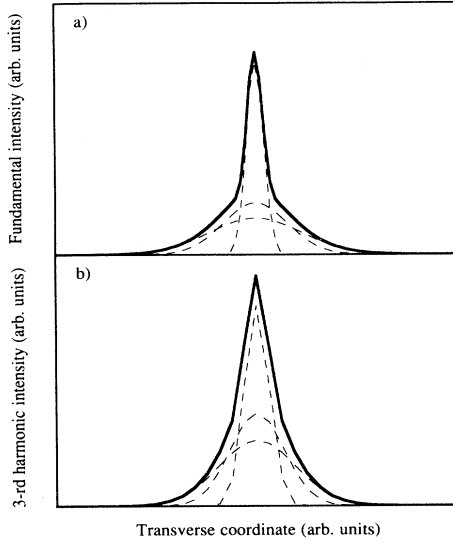
FIG. 2. Schematic patterns of (a) the fundamental u_1 and (b) the third-harmonic u_3 after the interaction with the pulsed atomic jet in the case of single scattering.

FIG. 3. Plot of the function $h(s)$ introduced in Eq. (37) and calculated by means of Eq. (56) with the mode amplitudes of Eq. (59).

dent one (see Fig. 2). When the saturation parameter is sufficiently small, the scattered field reduces to a single TEM$_{00}$ Gaussian beam, so that the pattern of the total field is composed of a main central lobe plus a weak and much broader scattered beam. Such a pattern has been observed experimentally as discussed in Sec. VI A. A more accurate expression of the field will be discussed in Sec. III A. In particular, the above picture of the field as a superposition of TEM$_{00}$ modes is confirmed by the modal expansion. The main difference with the exact analysis concerns the beamwidths. In practice, in (36) the coefficient p appearing in the argument of the exponential must be replaced by an effective p_k [see Eqs. (63)
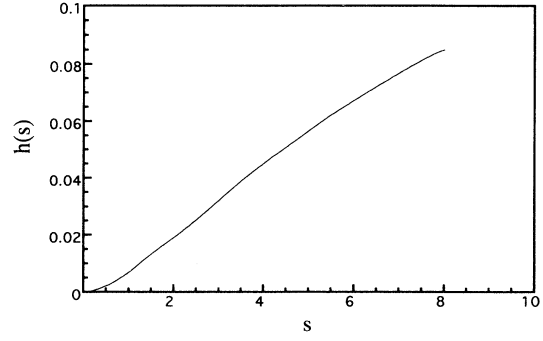
and (64)].

The fraction of the incident power scattered by the plasma is measured by the scattering cross section σ

$$\sigma = \pi w_0^2 \frac{P_{sc}}{P_{in}} \equiv \pi w_0^2 \Delta\phi^2 h(s) \tag{37}$$

with $h(s)$ a function of the saturation parameter plotted in Fig. 3. The above expression of σ can be extended to the incident ϵ_{in} and scattered ϵ_{sc} energies of a laser pulse having a temporal profile $\theta(t^*)$ by setting

$$\sigma_\epsilon = \pi w_0^2 \frac{\epsilon_{sc}}{\epsilon_{in}} = \frac{\int_{-\infty}^{\infty} \theta^2(t^*)\sigma[\mathcal{N}_{max}, s(t^*)]dt^*}{\int_{-\infty}^{\infty} \theta^2(t^*)dt^*}. \tag{38}$$

The scattered field is structured as a superposition of TEM$_{00}$ beams having divergences much larger than the incident one. If we measure the energy ϵ_t flowing outside the cone occupied by the unperturbed beam we have

$$\sigma_t \equiv \pi w_0^2 \frac{\epsilon_t}{\epsilon_{in}} = \pi w_0^2 \left\{ e^{-V_0} + \frac{\pi\Delta\phi^2}{4p^2} \sum_{k,k'=1}^{\infty} \frac{\frac{\int_{-\infty}^{\infty} \theta^2(t^*)(-s)^{k+k'} dt^*}{\int_{-\infty}^{\infty} \theta^2 dt^*}}{k!k'!\sqrt{(k+1)(k'+1)(k+k')}} \exp\left(-\frac{V_0}{4} \frac{p_k k + p_{k'} k'}{p_k k p_{k'} k'}\right) \right\}, \tag{39}$$

where $V_0 = k_1 b \rho_0^2/z^2$ with ρ_0 representing the radius of the stop used for eliminating the central lobe. When the order of nonlinearity p is sufficiently large, ρ_0 can be chosen in such a way as to make σ_t sufficiently close to σ_ϵ.

III. MODE EXPANSION

For calculating the field in the more general case we can integrate the wave equation by expanding the field in a superposition of TEM$_{m0}$ Gauss-Laguerre modes of confocal parameter B,

$$u_1^{(m)}(\rho, z) = \cos\Psi \, L_m(V)e^{-(1-i\tan\Psi)V/2-i(1+2m)\Psi}. \tag{40}$$

In Eq. (40) the coordinate ρ has been replaced by

$$V = \frac{k_1\rho^2}{B(1+z^2/B^2)} = \frac{k_1\rho^2}{B}\cos^2\Psi \tag{41}$$

with B representing the confocal parameter of the beams $u_1^{(m)}$ and the angle Ψ defined by the relation $z = B\tan\Psi$.

Representing the fundamental beam u_1 as a combination of the above modes

$$u_1(\mathbf{r}; t^*) = \sum_{m=0}^{\infty} E_1^{(m)}(\Psi; t^*) u_1^{(m)}(\mathbf{r}) \qquad (42)$$

amounts to associating u_1 with a vector $\mathbf{E}_1$ of components $E_1^{(m)}$. In particular, the TEM$_{00}$ beam of Eq. (9)

$$u_{\text{in}} = \cos\psi \; e^{-(1-i\tan\psi)v/2 - i\psi}, \qquad (43)$$

recast in terms of the variables ψ and v defined implicitly by the relations $z = b\tan\psi = B\tan\Psi$ and $v = k_1\rho^2\cos^2\psi/b = V(\cos^2\psi/\cos^2\Psi)(B/b)$, is represented by a vector of components [see Eq. (A8)]

$$E_1^{(m)}(\Psi) = \frac{\cos\psi}{\cos\Psi} e^{i(1+2m)\Psi - i\psi}(1-a)a^n, \qquad (44)$$

with $a = [(1 - i\tan\psi)v/V - 1 + i\tan\Psi]/[(1 - i\tan\psi)v/V + 1 + i\tan\Psi]$.

Now, plugging (42) into the parabolic wave equation (5) yields

$$\sum_m u_1^{(m)}\left(\frac{dE_1^{(m)}}{d\Psi} + i\Delta\Phi \; \cos^{-2}\Psi \; f \; E_1^{(m)}\right) = 0, \qquad (45)$$

where $\Delta\Phi = \Delta\phi B/b$. Next, multiplying Eq. (45) by $u_1^{(n)*}$, integrating over the cross section, and exploiting the orthogonality $[\int_0^\infty u_1^{(m)*}(V,\Psi)u_1^{(n)}(V,\Psi)dV = \delta_{m,n}\cos^2\Psi]$ of the modes $u_1^{(m)}$, we finally obtain

$$\frac{d}{d\Psi}E_1^{(n)} = -i\Delta\Phi \; \cos^{-2}\Psi \frac{\mathcal{N}(\Psi)}{\mathcal{N}_{\text{max}}}$$
$$\times \sum_m e^{2i(n-m)\Psi}M_1^{(m;n)}E_1^{(m)}, \qquad (46)$$

with $\mathbf{M}_1$ a symmetric matrix discussed in Appendix A,

$$M_1^{(m;n)} \equiv \frac{\mathcal{N}_{\text{max}}}{\mathcal{N}} \int_0^\infty e^{-V} L_n(V) L_m(V) f \, dV \qquad (47)$$

and f defined in Eqs. (18) and (20).

By virtue of the symmetry of $\mathbf{M}_1$, the modulus of $\mathbf{E}_1$ remains constant during the transport along the plasma axis.

Introducing the intensity matrix $\mathbf{I}_1$

$$I_1^{(m;n)}(\Psi; t^*) \equiv \int_0^\infty e^{-V} L_m(V) L_n(V) |u_1(V,\Psi;t^*)|^2 dV$$
$$= \sum_{k,l} C_{klmn} e^{2i(l-k)\Psi} E_1^{(k)} E_1^{(l)*}, \qquad (48)$$

with

$$C_{klmn} = \int_0^\infty e^{-2x} L_k(x) L_l(x) L_m(x) L_n(x) dx, \qquad (49)$$

$\mathbf{M}_1$ can be expressed as

$$\mathbf{M}_1(\Psi; t^*) = 1 - \exp\left[-s_{\text{max}}\frac{\int_{-\infty}^{t^*}\theta^{2p}(t')\mathbf{I}_1^p(\Psi; t')dt'}{\int_{-\infty}^{\infty}\theta^{2p}(t')dt'}\right]. \qquad (50)$$

Replacing $E_1^{(n)}$ by $\tilde{E}_1^{(n)} \equiv E_1^{(n)}e^{-2in\Psi}$, the system (46)

can be recast as

$$\frac{d}{d\Psi}\tilde{E}_1^{(n)} = -i2n\tilde{E}_1^{(n)} - i\Delta\Phi \; \cos^{-2}\Psi\frac{\mathcal{N}(\Psi)}{\mathcal{N}_{\text{max}}}$$
$$\times \sum_m M_1^{(m;n)}\tilde{E}_1^{(m)}. \qquad (51)$$

Patterns of the fundamental calculated by integrating the system (51) for different values of $\Delta\phi$ and s are presented in Fig. 4.

Implicit in the use of the parabolic wave equation (5) is the assumption that $|k_1 dE_1^{(n)}/dz| \ll |d^2E_1^{(n)}/dz^2|$. On the other hand, according to (46), $|dE_1^{(0)}/dz| \leq \Delta\nu_1|E_1^{(0)}|$. Since $\Delta\nu_{\text{max}}$ is of the order of 10^{-3}–10^{-4}, the condition that $E_1^{(n)}$ does not change significantly over one wavelength is well satisfied.

The scattering cross section σ [see (37)] is simply given by

$$\sigma = \pi w_0^2 |\mathbf{E}_{1(\text{out})} - \mathbf{E}_{1(\text{in})}|^2. \qquad (52)$$

Integrating the system (51) provides the amplitudes $\tilde{E}_{1(\text{out})}^{(m)}$ relative to the far field for given values of the saturation parameter $s(t^*)$. By dividing the pulse duration into several intervals (slots) and repeating the integration for the values of s relative to each time slot, the space-time profile of the far field is easily reconstructed.

The cross-section relative to the scattered energy [see Eq. (38)] will be given by

$$\sigma_\epsilon = \pi w_0^2 \frac{\int_{-\infty}^{\infty}\theta^2 dt|\mathbf{E}_{1(\text{out})} - \mathbf{E}_{1(\text{in})}|^2}{\int_{-\infty}^{\infty}\theta^2 dt}. \qquad (53)$$

In particular, the power $P_q(t^*)$ carried by the harmonic field at time t is proportional to the squared modulus of $\mathbf{E}_{q(\text{out})}$,

$$P_q(t) = (\pi q k b 2^{1-q})^2\mathcal{N}_{\text{max}}^2\chi_{\text{at}}^{(q)2}I^q\theta^{2q}(t)|\mathbf{E}_{q(\text{out})}|^2. \qquad (54)$$

On the other hand, as shown in Appendix D, the aperture of the harmonic field also can be expressed in terms of these coefficients.

A. Perturbative integration of the equation of motion of $\mathbf{E}_1$

Before concluding this section we shall dwell on the integration of the differential system for very small values of $\Delta\Phi$. To this end we represent $\mathbf{E}_1$ as an asymptotic series in the smallness parameter $\Delta\phi$,

$$\mathbf{E}_1 = \mathbf{E}_1^{(0)} + \Delta\phi\mathbf{E}_1 + \Delta\phi^2\mathbf{E}_1^2 + \cdots. \qquad (55)$$

The zeroth-order vector $\mathbf{E}_1^{(0)}$ coincides with the incident field. Accordingly, the cross section σ can be expressed as [see Eq. (52)]

$$\sigma = \pi w_0^2(\Delta\phi)^2|\mathbf{E}_{1(\text{out})} + \Delta\phi\mathbf{E}_{1(\text{out})}^2 + \cdots|^2. \qquad (56)$$

The quadratic dependence of σ on the particle density for small values of $\mathcal{N}_{\text{max}}$ is a consequence of the fact that this scattering process is coherent, as implicitly assumed in the wave equation (5). This fact has been confirmed

experimentally by the measurement of σ in conditions of single scattering (see Sec. VI B).

$\mathbf{E}_1^1$ can be determined by integrating the system (46) by plugging $\mathbf{E}_1^0$ into the right-hand side. Choosing $B = b$ and assuming that the ionization is produced by the TEM$_{00}$ beam of Eq. (9), the derivative of $E_1^{1(n)}$ reads [see Eq. (A6)]

$$\frac{d}{d\psi} E_1^{1(n)} = -i \frac{\mathcal{N}(\psi)}{\mathcal{N}_{\max}} \sum_{k=1}^{\infty} \frac{(-s)^k}{k!} \cos^{2kp-2} \psi \; e^{i2n\psi}$$

$$\times \frac{1}{(1+1/kp)^n} \frac{1}{1+kp}. \tag{57}$$

Expressing $\mathcal{N}/\mathcal{N}_{\max}$ by means of the series (32) and relying on (33) gives
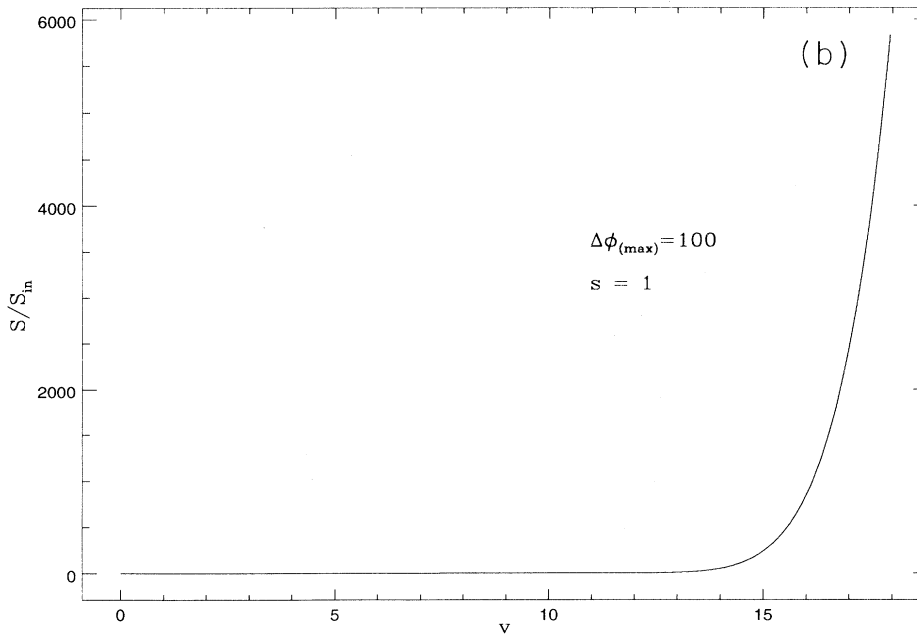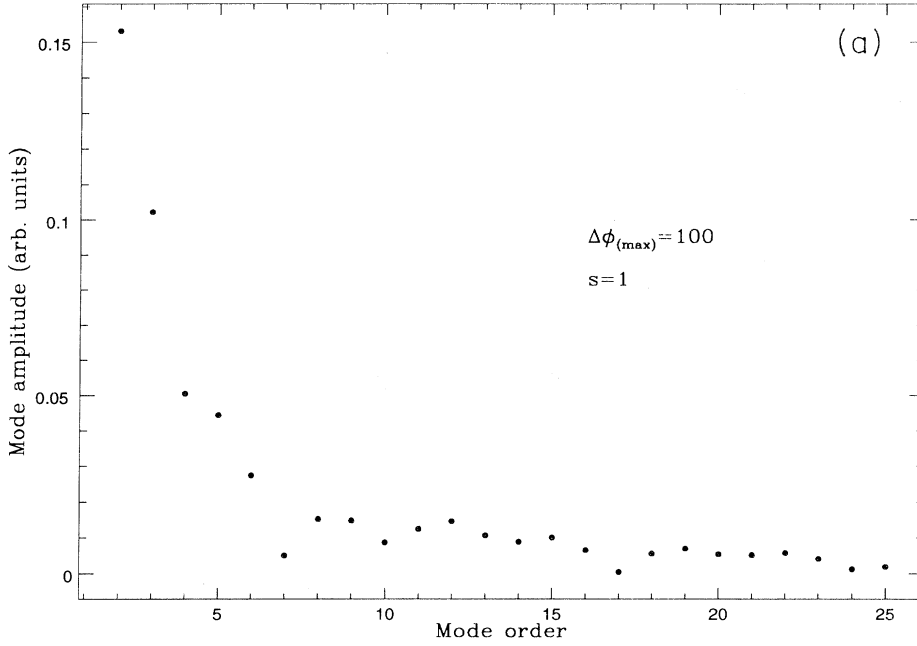
FIG. 4. (a) Mode amplitudes $|E_{1(\text{out})}^{1(n)}|$ $(n = 0, 1, ..., 25)$ calculated by integrating the differential system (51) for a constant particle number density and for $\Delta\phi=100$ and $s = 1$. The matrix $\mathbf{M}_1$ has been evaluated by means of Eq. (50) with the intensity matrix $\mathbf{I}_1$ of Eq. (48). (b) Ratio $S(v)/S_{\text{in}}(v)$ of the intensity S divided by the intensity S_{in} of the incident beam. Notice the rapid increase of the ratio for $v \geq 15$.

$$E_1^{1(n)} = -\sum_{k=1}^{\infty} \frac{(-s)^k}{k!} \frac{1}{1+kp} \frac{1}{(1+1/kp)^n}$$

$$\times \left[\sum_{lm}{}' N_l c(kp+l-1,m) \frac{e^{i2(n-m)\psi} - (-1)^{n-m}}{2(n-m)} + i(\psi+\pi/2) \sum_l N_l c(kp+l-1,n) \right]$$

$$\equiv \sum_{k=1}^{\infty} \frac{(-s)^k}{k!} E_1^{1(k)(n)}, \tag{58}$$

where the sum $\sum'_{lm}$ is extended to $m \neq n$. In particular,

$$E_{1(\text{out})}^{1(n)} = -i\pi \sum_{k=1}^{\infty} \frac{(-s)^k}{k!} \frac{1}{1+kp} \frac{1}{(1+1/kp)^n}$$

$$\times \sum_{l=0}^{\infty} N_l c(kp+l-1,n). \tag{59}$$

Summing the above series for a uniform particle distribution and using a best fit up to n^3 for $n \leq 50$ we obtain [see Figs. 5(a) and 5(b)]

$$E_1^{1(n)} \approx -i0.033 \times 0.429^{n+0.00188n^2-1.4\times10^{-4}n^3}$$

$$\text{for } s = 1,$$

$$E_1^{1(n)} \approx -i0.053 \times 0.446^{n+0.00136n^2+3.72\times10^{-5}n^3}$$

$$\text{for } s = 2. \tag{60}$$

As discussed in Sec. II [see Eq. (36)], in the limit of the Born approximation the scattered field is formed by a superposition of Gaussian TEM_{00} beams $\mathbf{E}_{1(\text{out})} = \mathbf{E}_{\text{in}} + \mathbf{E}_1^{(1)} + \mathbf{E}_1^{(2)} + \cdots$, with different beamwidths. In terms of modes, $\mathbf{E}_{1(\text{out})}^1$ has components

$$E_{1(\text{out})}^{1(n)} \propto -i \sum_{k=1}^{\infty} \frac{(-s)^k}{k!} \frac{1}{kp} \left(\frac{2kp-1}{2kp+1} \right)^n$$

$$\times \sum_l N_l c(kp+l-1,0). \tag{61}$$

The above expression differs from (59) by the presence of the factors $c(kp+l-1,0)$ instead of $c(kp+l-1,n)$. The different behavior is due to the phase factors $e^{i2(n-m)\Psi}$ in front of the matrix $\mathbf{M}_1$ in Eq. (46). The patterns relative to Eqs. (59) and (61) are qualitatively similar, but differ notably for the divergence (see Fig. 6). This discrepancy can be removed by using suitable power distributions. Representing the vector $\mathbf{E}_{1(\text{out})}^1$ in the form $\mathbf{E}_{1(\text{out})}^1 = \sum_{k=1}^{\infty} \frac{(-s)^k}{k!} \mathbf{E}_{1(\text{out})}^{1(k)}$, we approximate $\mathbf{E}_{1(\text{out})}^{(k)}$ by the power law

$$E_{1(\text{out})}^{1(k)(n)} \approx E_{1(\text{approx})}^{1(k)(n)} = x^{(k)} \frac{c(kp+l-1,0)}{1+kp} y^{(k)n}. \tag{62}$$

Minimizing the distance $|\mathbf{E}_{1(\text{out})}^{1(k)} - \mathbf{E}_{1(\text{approx})}^{1(k)}|^2$ we obtain for $p=12$ and for a uniform particle distribution
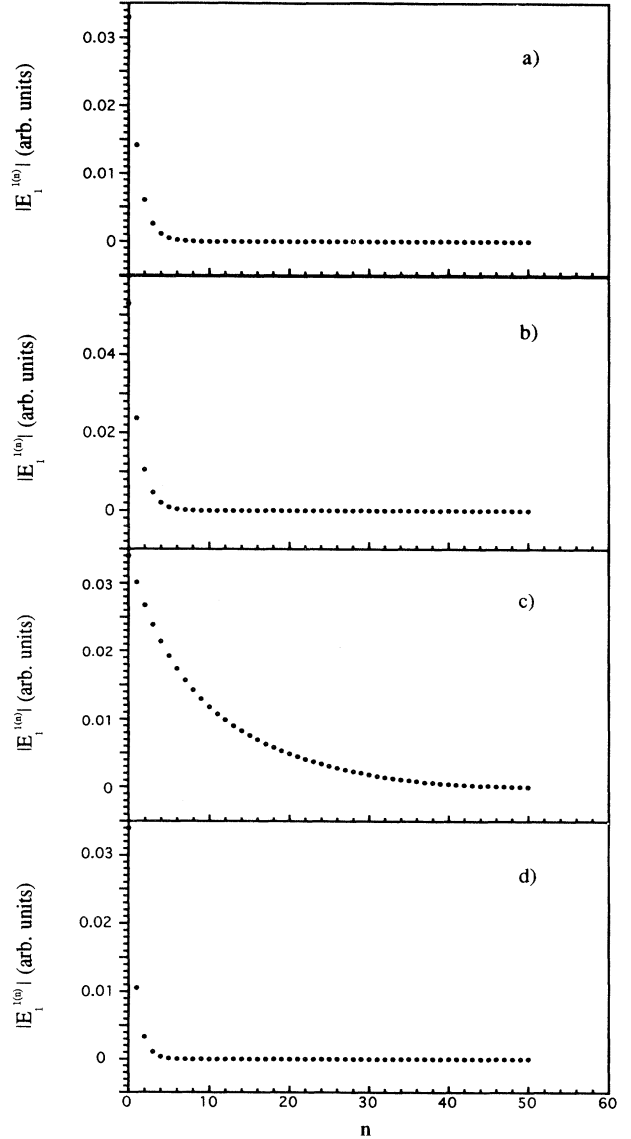

FIG. 5. (a) Mode amplitudes $|E_{1(\text{out})}^{1(n)}|$ ($n = 0, 1, ..., 50$) calculated by means of Eq. (59) for a small value of $\Delta\phi$ and $s = 1$; (b) same as (a) but for $s = 2$; (c) same as for (a) but with modes given by (61) and $s = 1$; (d) same as for (a) but with modes relative to $B = 0.5b$.

$$x^{(1)} = 1.0948, \quad y^{(1)} = 0.672,$$
$$x^{(2)} = 1.1315, \quad y^{(2)} = 0.760,$$
$$x^{(3)} = 1.1507, \quad y^{(3)} = 0.801,$$
$$x^{(4)} = 1.1631, \quad y^{(4)} = 0.826, \qquad (63)$$
$$x^{(5)} = 1.1719, \quad y^{(5)} = 0.843,$$
$$x^{(6)} = 1.1787, \quad y^{(6)} = 0.856,$$

with a residual error $|\mathbf{E}_{1(out)}^{1(k)} - \mathbf{E}_{1(approx)}^{1(k)}|^2 / |\mathbf{E}_{1(out)}^{1(k)}|^2 \leq 0.027$. Accordingly, the field of Eq. (36) is superseded by

FIG. 6. Patterns relative to the mode distributions (a) (59) and (b)–(d) (61) for $k = 1$. (b)–(d) have been calculated by summing $N = 20, 40$, and 60 modes, respectively.

$$u_1(\mathbf{r}; t^*) \propto \exp\left(-\frac{v}{2}\right)$$
$$+ i\Delta\phi \sum_{k=1}^{\infty} \frac{(-s)^k}{k!} \frac{x^{(k)}}{kp} c(kp - 1, 0)$$
$$\times \exp\left(-\frac{v}{2} \frac{y^{(k)} - 1}{y^{(k)} + 1}\right). \qquad (64)$$

For improving the convergence of the series (42) it is worth choosing $B \neq b$. For example, with $B = 0.5b$ we obtain the amplitude distribution of Fig. 5(d), which is approximated by the best fit

$$E_1^{1(n)} \approx -i\, 0.034 \times 0.311^{n - 0.009n^2 + 6.67 \times 10^{-5} n^3}$$

$$\text{for } s = 1, \quad (65)$$

IV. HARMONIC FIELD

The harmonic-generation problem has been analyzed by L'Huillier *et al.* [1, 3, 4] by starting from the wave equations for the envelope $\mathcal{E}_p$ of the harmonic fields

$$\left(\nabla_\perp^2 + 2iqk_1\frac{\partial}{\partial z} + 2(qk_1)^2\Delta\nu_q\right)\mathcal{E}_q = -4\pi(qk_1)^2\mathcal{P}_q. \qquad (66)$$

$\Delta\nu_q = \Delta\nu_1/q^2$ represents, as for the fundamental, the deviation from unity of the refractive index at the harmonic frequencies. The subscript q refers to the qth-harmonic beam throughout.

The envelope $\mathcal{P}_q$ of the polarization field is a function of $\mathcal{E}_1$, which reduces, in the weak field case, to the qth power of the laser field amplitude $\mathcal{E}_1$. If we neglect the propagation time through the ionized region, the time-dependent polarization will be given by

$$\mathcal{P}_q(\Psi, V; t^*) = 2^{1-q}\mathcal{N}\chi^{(q)}I^{q/2}\theta^q u_1^q(\Psi, V)$$
$$\equiv \mathcal{P}_{q(\Phi\max)}(t^*)\frac{\mathcal{N}(\Psi)}{\mathcal{N}_{\max}}u_1^q, \qquad (67)$$

with $\chi^{(q)}$ the nonlinear susceptibility [4]

$$\chi^{(q)} = \frac{\mathcal{N}_{at}}{\mathcal{N}}\chi_{at}^{(q)} + \frac{\mathcal{N}_{ion}}{\mathcal{N}}\chi_{ion}^{(q)} = \chi_{at}^{(q)}(1 - f_e) + \chi_{ion}^{(q)}f_e, \qquad (68)$$

with $f_e = \mathcal{N}_e(\Psi, V; t^*)/\mathcal{N}(\Psi) = f\mathcal{N}_{\max}/\mathcal{N}(\Psi)$.

Lago *et al.* [2] and L'Huillier *et al.* [1, 3, 4], following the approach of Refs. [14–16], have calculated the harmonic field by expressing it as an integral over the polarization field. Here we prefer a different approach based on the representation of $\mathcal{E}_q$ as a combination of modes

$$u_q^{(m)}(qV, \Psi) = \cos\Psi\, L_m(qV)e^{-(1 - i\,\tan\Psi)qV/2 - i(1 + 2m)\Psi}. \qquad (69)$$

Plugging into Eq. (66) the right-hand side of the expansion

$$\mathcal{E}_q(\mathbf{r}; t^*) = 2\pi k_1 B\mathcal{P}_{\max}(t^*)u_q(\mathbf{r}, t^*)$$
$$= 2\pi k_1 B\mathcal{P}_{q(\max)}(t^*)\sum_m E_q^{(m)}(\Psi, t^*)u_q^{(m)}(\mathbf{r}) \qquad (70)$$

we obtain [see Eq. (46)]
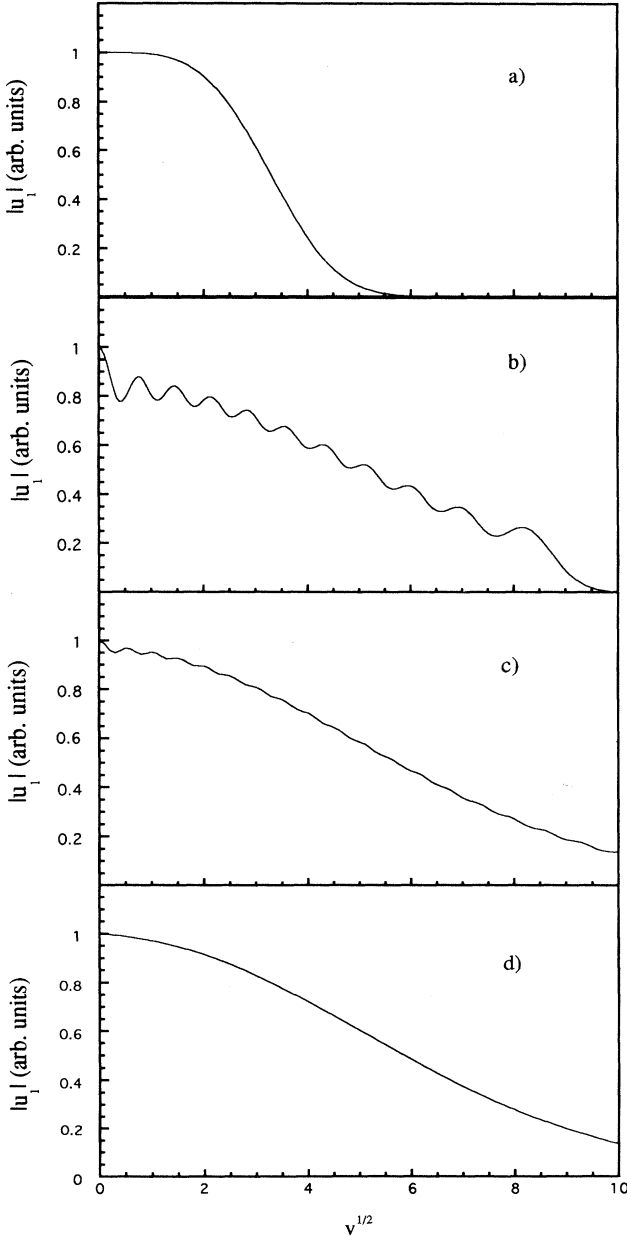
$$\frac{d}{d\Psi}E_q^{(n)} = -i\Delta\Phi\,\cos^{-2}\Psi\,\frac{\mathcal{N}}{\mathcal{N}_{\max}}\sum_m e^{i2(n-m)\Psi}$$
$$\times M_q^{(m;n)}E_q^{(m)}$$
$$+i\,\cos^{q-3}\Psi e^{i(2n-q+1)\Psi}\frac{\mathcal{N}}{\mathcal{N}_{\max}}S_q^{(n)}, \qquad (71)$$

where

$$M_q^{(m;n)} \equiv \frac{\mathcal{N}}{\mathcal{N}_{\max}}\int_0^\infty e^{-qV}L_m(qV)L_n(qV)f(\Psi,V)dV,$$

$$S_q^{(n)} \equiv \sum_{i_1,i_2,\ldots,i_q;n}C_{i_1,i_2,\ldots,i_q;n}\tilde{E}_1^{(i_1)}\tilde{E}_1^{(i_2)}\cdots\tilde{E}_1^{(i_q)}, \qquad (72)$$

with

$$C_{i_1,i_2,\ldots,i_q;n} = \int_0^\infty e^{-qx}L_{i_1}(x)L_{i_2}(x)\cdots L_{i_q}L_n(qx)dx. \qquad (73)$$

The first term on the right-hand side of (71) describes the effects of the plasma on the propagation of the qth harmonic. The second one represents the polarization source proportional to the qth power of the incident field. In Fig. 7 we have plotted two typical patterns of the third harmonic calculated by integrating the differential system (71).

A. Perturbative integration of the equation of motion of $\mathbf{E}_q$

If we expand $\mathbf{E}_q$ in an asymptotic power series in $\Delta\phi$,

$$\mathbf{E}_q = \mathbf{E}_q^0 + \Delta\phi\mathbf{E}_q^1 + \cdots, \qquad (74)$$

assuming $B = b$ we obtain from (71)

$$\frac{d}{d\psi}E_q^{0(n)} = i\delta_{n0}\sum_l N_l\cos^{2l+q-3}\psi e^{i(-q+1)\psi}. \qquad (75)$$
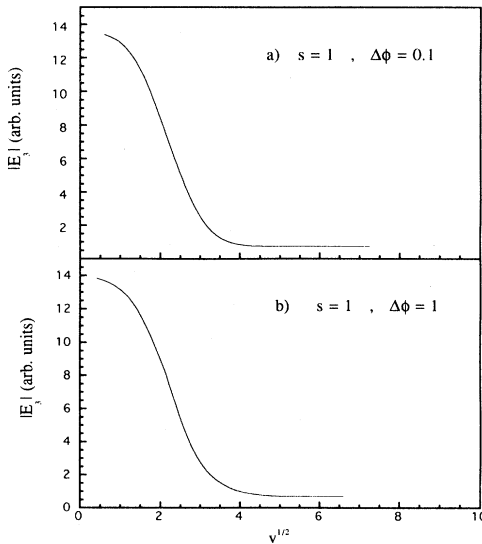
FIG. 7. Patterns of the third-harmonic field amplitude obtained by integrating the differential system (71) for different values of $\Delta\phi$ and s. (a) $\Delta\phi = 0.1$, $s = 1$; (b) $\Delta\phi = 1$, $s = 1$.

Then

$$E_q^{0(0)} = \sum_{l,\mu}{}'N_lc\left(l+\frac{q-3}{2},\mu\right)$$
$$\times\frac{e^{i(2\mu-q+1)\psi}-(-1)^{\mu-\frac{q-1}{2}}}{2\mu-q+1}$$
$$+\frac{i}{2}(\psi+\pi/2)\sum_l N_lc\left(l+\frac{q-3}{2},\frac{q-1}{2}\right), \qquad (76)$$

the sum $\sum_{l\mu}'$ being extended to positive and negative integers $\mu \neq (q-1)/2$. In the absence of the electron plasma the qth harmonic is a TEM_{00} beam with far-field amplitude

$$E_{q(\text{out})}^{0(0)} = i\pi\sum_{l=1}^\infty N_lc\left(l+\frac{q-3}{2},\frac{q-1}{2}\right). \qquad (77)$$

In particular, $E_{q(\text{out})}^{0(0)}$ vanishes for a uniform particle distribution.

For a Lorentzian distribution $\mathcal{N}/\mathcal{N}_{\max} = 1/(1+\tan^2\psi/\tan^2\psi_0)$ with $|\tan^2\psi_0 - 1| < 1$,

$$E_{q(\text{out})}^{0(0)} = i\pi\,\tan^2\psi_0\sum_{l=1}^\infty(1-\tan^2\psi_0)^{l-1}$$
$$\times c\left(l+\frac{q-3}{2},\frac{q-1}{2}\right). \qquad (78)$$

At first order in $\Delta\phi$, $S_q^{(n)}$ reduces to $\Delta\phi\sum_m C_{0,0,\ldots,0m;n}\tilde{E}_1^{1(m)}$. Since $C_{0,0,\ldots,m;n} = \binom{m}{n}(q-1)^{m-n}/q^{m+1}$, Eq. (71) gives

$$\frac{d}{d\psi}E_q^{1(n)} = -i\,\cos^{-2}\psi\frac{\mathcal{N}}{\mathcal{N}_{\max}}M_q^{(0;n)}e^{2in\psi}E_q^{0(0)}$$
$$+i\frac{\mathcal{N}}{\mathcal{N}_{\max}}\sum_{m\geq n}\frac{(q-1)^{m-n}}{q^m}\binom{m}{n}$$
$$\times\cos^{q-3}\psi e^{i(2n-2m-q+1)\psi}E_1^{1(m)}. \qquad (79)$$

The first term on the right-hand side of (79) represents the contribution of the aberration undergone by the qth harmonic. The second term is due to the aberration undergone by the incident field. Accordingly, the effect of the plasma on the harmonic is twofold: a direct aberration of the harmonic field propagating through the nonhomogeneous ionized medium and an aberration caused by the aberrated fundamental beam. It is worth noting that $E_q^{1(n)}$ depends only on the modes of the fundamental of order greater than $n-1$.

Now, expanding $E_q^{1(n)}$ in a power series in the saturation parameter [see Eq. (58)]

$$E_q^{1(n)} = \sum_{k=1}^\infty\frac{(-s)^k}{k!}E_q^{1(k)(n)} \qquad (80)$$

and integrating Eq. (79) for the kth-order mode amplitudes we obtain for $q = 3$ (see Appendix D)

$$i\frac{2}{\pi}E_{3(\text{out})}^{1(k)(n)} = \frac{1}{kp/3+1}\frac{1}{(1+3/kp)^n}\sum_l N_l\left[\sum_{l'\mu}{}'N_{l'}c(l',\mu)\frac{c(kp+l-1,\mu+n-1)-(-1)^{\mu-1}c(kp+l-1,n)}{\mu-1}\right.$$

$$+\sum_{l'}N_{l'}c(l',1)\left(\sum_\mu{}'\frac{(-1)^{n-\mu}}{n-\mu}c(kp+l-1,\mu)+i\pi c(kp+l-1,n)\right)\Bigg]$$

$$+\frac{1}{1+kp}\frac{1}{(3+3/kp)^n}\sum_{lm}N_l\binom{m}{n}\left(\frac{2}{3+3/kp}\right)^{m-n}$$

$$\times\left[\sum_{l'\mu}{}'N_{l'}c(kp+l'-1,\mu)\frac{c(l,\mu-n+1)-(-1)^{m-\mu}c(l,m-n+1)}{m-\mu}\right.$$

$$+\sum_{l'}N_{l'}c(kp+l'-1,m)\left(\sum_\mu{}'\frac{(-1)^{n-m-1-\mu}}{n-m-1-\mu}c(l,\mu)+i\pi c(l,m-n+1)\right)\Bigg]. \tag{81}$$

In particular, for a particle Lorentzian distribution with $\psi_0 = \pi/4$ [cf. (78)]

$$i\frac{8}{\pi}E_{3(\text{out})}^{(n)} = -2\delta_{n0} + \Delta\phi\sum_k\frac{(-s)^k}{k!}\left\{\frac{1}{kp/3+1}\frac{1}{(1+3/kp)^n}[-d(kp,n)+i\pi c(kp,n)]\right.$$

$$\left.+\frac{1}{kp+1}1(3+3/kp)^n[d(kp,n)+i\pi c(kp,n)+e(kp,n)]\right\}, \tag{82}$$

where

$$d(kp,n) = 1.5c(kp,n) + 2c(kp,n-1) + 0.5c(kp,n-2) + \sum_\mu{}'\frac{(-1)^{\mu-n}}{\mu-n}c(kp,\mu),$$

$$e(kp,n) = \sum_{m=n+1}^\infty\binom{m}{n}\left(\frac{2}{3+3/kp}\right)^{m-n}\left[\frac{c(kp,n)}{m-n}+2\frac{c(kp,n-1)}{m-n+1}+\frac{c(kp,n-2)}{m-n+2}\right.$$

$$\left.+2\frac{(-1)^{n-m}c(kp,m)}{[(n-m-1)^2-1](n-m-1)}\right]. \tag{83}$$

Summing the above series and using a best fit up to n^3 for $n \le 20$ we obtain for $s=1$

$$|E_3^{1(n)}| \approx 0.043 \times 0.171^{n-0.0457\,n^2+1.22\times10^{-3}n^3}. \tag{84}$$

Since $E_3^{0(0)} = 0.5$ and in view of these values of $E_3^{1(n)}$, we can truncate to first order the series expansion of the mode amplitudes for $\Delta\phi$ no greater than 10.

In Fig. 8 we have plotted the third-harmonic pattern for $\mathcal{N}/\mathcal{N}_{\text{max}} = \cos^2\psi$, $s=1$, and $\Delta\phi = 1,3,5,6$. The broadening of the beam is evident for increasing $\Delta\phi$. Finally, we can estimate the effective beamwidth θ of the harmonic beam by means of Eq. (E3)

$$\frac{\theta^2}{\theta_0^2} = \frac{\Delta\phi^2\sum_{n=0}^\infty\{2(n+1)\text{Re}(\hat{E}_{q(\text{out})}^{1(n+1)}\hat{E}_{q(\text{out})}^{1(n)})+(2n+1)|\hat{E}_{q(\text{out})}^{1(n)}|^2\}+2\Delta\phi\text{Re}(\hat{E}_{q(\text{out})}^{1(0)}+\hat{E}_{q(\text{out})}^{1(1)})+1}{\Delta\phi^2\sum_{n=0}^\infty|\hat{E}_{q(\text{out})}^{1(n)}|^2+2\Delta\phi\text{Re}\hat{E}_{q(\text{out})}^{1(0)}+1}, \tag{85}$$

with $\hat{E}_{q(\text{out})}^{1(n)} \equiv E_{q(\text{out})}^{1(n)}/E_{q(\text{out})}^{0(0)}$ and θ_0 the beamwidth in the absence of aberrations.

B. Integral expression of the far-field mode amplitudes

As an alternative to Eq. (69) we can expand the field in terms of modes $U_q^{(r)}$ satisfying the homogeneous wave equation

$$\left(\nabla_\perp^2 + 2iqk_1\frac{\partial}{\partial z} + 2(qk_1)^2\Delta\nu_q\right)U_q^{(r)} = 0 \tag{86}$$

and reducing as $z \to \infty$ to the TEM$_{r0}$ Gaussian mode $u_q^{(r)}$. From the Green's theorem applied to Eq. (80) we find that

$$\frac{d}{dz}\int_0^\infty U_q^{(s)}U_q^{(r)*}d\rho^2 = 0. \tag{87}$$

Since for $z \to \infty$, $U_q^{(r)}$ and $U_q^{(s)}$ reduce respectively to the mutually orthogonal modes TEM$_{r0}$ and TEM$_{s0}$, then the modes $U_q^{(r)}$ are mutually orthogonal at every section.

These modes $U_q^{(r)}$ can be used as basis for representing the harmonic field

$$\mathcal{E}_q(\Psi, V; t^*) = 2\pi k_1 B \mathcal{P}_{q(\max)}(t^*)$$
$$\times \sum_r F_q^{(r)}(\Psi; t^*) U_q^{(r)}(\Psi, V; t^*). \quad (88)$$

The coefficients $F_q^{(r)}(\Psi; t^*)$ form a vector $\mathbf{F}_q$, which reduces to $\mathbf{E}_{q(\text{out})}$ in the far field. Using this representation, the nonhomogeneous parabolic equation (66) transforms into a transport equation [see Appendix B, Eq. (B6)] for $\mathbf{F}_q$.

The coefficients $F_{q(\text{out})}^{(r)} = E_{q(\text{out})}^{(r)}$ are a generalization of the phase-matching integrals used by L'Huillier *et al.* [1, 3, 4]: they represent the efficiency of generation in the far field of the Gaussian mode TEM_{r0}. It is shown in Appendix B that $E_{q(\text{out})}^{(r)}$ is given by

FIG. 8. Patterns of the third-harmonic intensity calculated by means of Eq. (82) for $s = 1$ and $\Delta\phi = 0.5, 1, 3, 5, 6$.

$$E_{q(\text{out})}^{(r)}(t) = iq\pi W_0^2 \int_{-\pi/2}^{\pi/2} \frac{\mathcal{N}}{\mathcal{N}_{\max}} \; g_q^{(r)} \; \cos^{q-3}\Psi d\Psi, \quad (89)$$

with

$$g_q^{(r)}(\Psi; t^*) = \cos^{-q-1}\psi \int_0^\infty \left(1 - f_e + \frac{\chi_{\text{ion}}^{(q)}}{\chi_{\text{at}}^{(q)}} f_e\right)$$
$$\times U_q^{(r)*} u_1^q dV. \quad (90)$$

V. EXPERIMENTAL SETUP

The light source used in our experiment is a mode-locked Nd:YAG laser (where YAG denotes yttrium aluminum garnet) ($\lambda = 1064$ nm), with two-stage amplification, delivering 35 ps/50 mJ pulses at a 10-Hz repetition rate. The laser pulse energy is varied by means of a half-wave plate–polarizer optical system and measured by a pyroelectric calorimeter. The laser beam is linearly polarized in the horizontal plane and focused on the gas target by an $f = 250$ mm focal length lens, which produces a confocal parameter b of about 5 mm (see Fig. 9).

The gas sample (Ar and Xe) is injected into the interaction chamber by a solenoid valve with a 0.8-mm orifice. With an opening time of about 1 ms and a backup pressure around 5 atm, the local pressure in the interaction volume ranges between 30 and 100 Torr. The interaction chamber can be pumped down by a turbomolecular pump to a background pressure of 2×10^{-8} Torr. With the valve operating at a few hertz the background pressure in the scattering chamber is about 3×10^{-2} Torr.

The gas jet characteristics (local pressure, density profile) have been determined with an interferometric method derived from the apparatus described by Faris and Hertz [17]. We can briefly say here that the gas jet profile can be approximated with a Lorentzian shape (in a plane orthogonal to the valve axis) whose full width at half maximum shows a linear dependence on the distance from the valve orifice, with a half angle of about 25°. The average pressure $\langle p \rangle$ experienced by the laser beam across the gas jet follows an exponential law

$$\langle p \rangle = \langle p_0 \rangle \; e^{-d/d_0}, \quad (91)$$

where d is measured along the valve axis. This result agrees with that reported by Lompré *et al.* [18]. The values of $\langle p_0 \rangle$ and d_0 deduced from a best fit of the experimental data for argon are, respectively, 90 Torr and 500 μm for a backup pressure of 10 atm. Most of the results reported in this paper have been obtained at a distance of about 500 μm from the nozzle and with backup pressures ranging between 1 and 10 atm of argon. We have verified that the local pressure is proportional to the backup pressure. In particular, for a backup pressure of ≈ 10 atm the local pressure is of the order of 40 Torr.

The uv light has been analyzed along the laser axis by using a nearly normal incidence (deflection angle $\delta = 15°$) grating monochromator, as shown in Fig. 9. As usual, in order to optimize the collection efficiency, the laser focus plays the role of the entrance slit of the monochromator. We have used in our experiment a Pt-coated, spherical holographic grating (Jobin-Yvon) with a radius of cur-
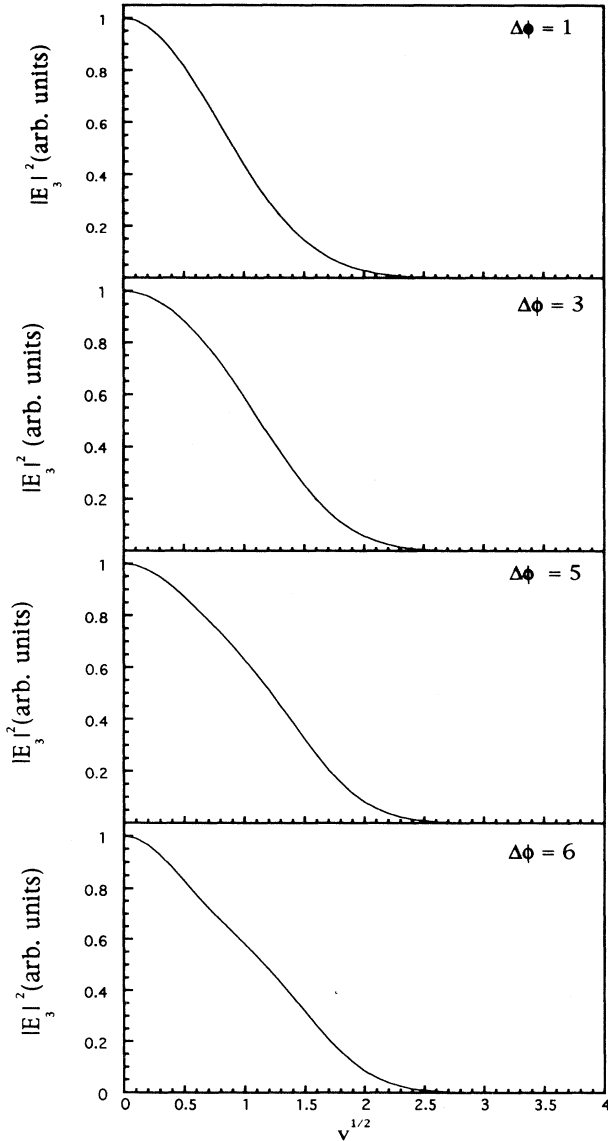
FIG. 9. Schematic view of the experimental setup. The Nd:YAG laser beam is focused by the lens L_1 ($f=$ 250 mm) onto the gas jet inside the scattering chamber S. The radiation escaping from S (aberrated incident beam plus harmonic field) is sent to the spherical grating G (1080 grooves/mm, blazed at 250 nm) and focused on the exit plane. A CCD camera is used for recording the pattern. A He-Ne is used for operating a differential interferometer [17]. The polarized input beam goes through a $\lambda/2$ plate and a cylindrical lens L_2. A spherical confocal mirror M_1 is used for obtaining a sheet of light that passes through the atomic jet. The output is sent to the calcite crystal C, tilted by the small angle θ. The two polarizations of the beam, spatially separated, interfere at the exit of the polarizer P. The interference pattern is analyzed by the photodiode PD mounted on a translation stage.

vature of 1 m and 22% spectral efficiency at the third harmonic ($\lambda = 355$ nm) of the laser fundamental.

The nearly normal incidence geometry of Fig. 9 has been chosen in order to reduce the aberrations introduced by the grating. In this case, when both the source and its image created by the spherical reflecting surface lie on the Rowland circle, the main residual aberration is astigmatism: the point source is imaged in two segments, one on the Rowland circle and normal to it (horizontal focus) and the other lying on the incidence plane and on the tangent to the Rowland circle through the source (vertical focus). As a consequence, the intensity distribution of the diffracted radiation in a generic plane normal to the diffraction direction has an elliptical profile.

Measurements of the third-harmonic beam profile and divergence angle in different experimental conditions have been performed by using a charge coupled device (CCD) detector (Pulnix TM 745 E) at various distances from the monochromator exit slit. The sensitive area of the CCD detector is 8.8× 6.6 mm^2 and consists of 780 (horizontal) by 244 (vertical) picture cells. The quantum efficiency of the CCD detector in the uv region is of the order of 10%, although it drastically decreases towards 200 nm. Finally, the precise determination of the harmonic power dependence on the laser intensity has been performed by using a photomultipier (Thorn-EMI 9250-QB) with quantum efficiency of about 25% at the third-harmonic wavelength. The experimental determination of the dramatic defocusing effects on the fundamental laser beam after its interaction with the ionized gas produced in the focal region is described in the following section.

VI. EXPERIMENTAL RESULTS

The results presented in this section refer mainly to argon as the target gas, although the main features have also been confirmed in the case of xenon. Moreover, we have concentrated our attention on the laser fundamental and its third harmonic only, because the detection response of our CCD camera is rather poor in the region

of the fifth harmonic ($\approx$200 nm). Nonetheless, we think that the experimental data reported in the following represent a significant test of the analytical model discussed in the previous sections. They can thus be extended to some extent to higher-order harmonics, particularly in the spectral region between the third and eleventh harmonics ($\approx$100–350 nm).

Another interesting aspect of our measurements is that they shed light on a very important feature of harmonic generation in noble gases with intense laser pulses: the laser-plasma interaction. In fact, a high gas pressure is desirable since the number of harmonic photons scales quadratically with gas density [19]. However, as well evidenced by our results, moving to higher gas densities certainly complicates the picture because of the interaction between the laser pulse and the ionized gas medium. This interaction has significant consequences from the point of view of the optical characteristics of the vacuum ultraviolet (vuv) radiation produced and can thus play an important role in specific applications. This turns out to be true even in the relatively moderate laser intensity range investigated in our experiment, namely, $10^{12}-10^{14}$ W cm^{-2}.

A. Defocusing of the fundamental beam

An important point of our analysis is the study of the effects that the laser radiation-plasma interaction has on the fundamental beam. To this end, we have carried out an experiment similar to the one reported by Auguste et al. [7], where the radiation produced by a terawatt laser was focused in a cell uniformly filled with helium at relatively high pressure (15 Torr to 1 atm). On the other hand, we have used an argon gas jet with local pressures of about 40 Torr, i.e., rather smaller than the ones of the above paper and, more important, of much lower laser intensities (about 10^{13} W cm^{-2} against $10^{15} - 10^{17}$ W cm^{-2}).

We have thus measured the laser pulse energy at the output of the vacuum chamber with a joule meter positioned just after a variable circular diaphragm and at a

distance from the focal volume equal to the focal length (25 cm) of the focusing lens. What we have observed is that the laser pulse energy transmitted after the interaction with the ionized gas decreases dramatically when the laser energy and/or the local gas pressure is increased. Figure 10 shows the energy transmission ratio, defined as ϵ_t/ϵ_{in}, where ϵ_t is the output energy and ϵ_{in} the incident one, as a function of the incident laser pulse energy at a fixed local pressure of the argon jet ($\simeq$ 40 Torr). Cases (a), (b), and (c) refer, respectively, to diaphragm diameters of 3 mm, 10 mm, and 20 mm (the unperturbed laser beam diameter is about 20 mm). Thus the defocusing effects on the fundamental beam are dramatic, with up to about 50% of the input energy diverted from the beam after laser-plasma interaction, and it is active on the whole laser beam cross section, even at the relatively moderate intensities of our experiment. It is worth noting that the pulse energies used in Fig. 10 are always smaller than that ($\simeq$ 20 mJ in our case) corresponding to the saturation intensity for argon ionization.

We have also studied the transmission ratio as a function of the local gas pressure, at fixed laser energy. By increasing the argon pressure in the range 20 − 50 Torr we have observed a consistent decrease in the transmitted energy, as shown in Fig. 11 for a laser energy of 15 mJ and the maximum diaphragm diameter (20 mm). Such a drop-off is fairly linear in the investigated pressure range, in good agreement with the corresponding results of Au-
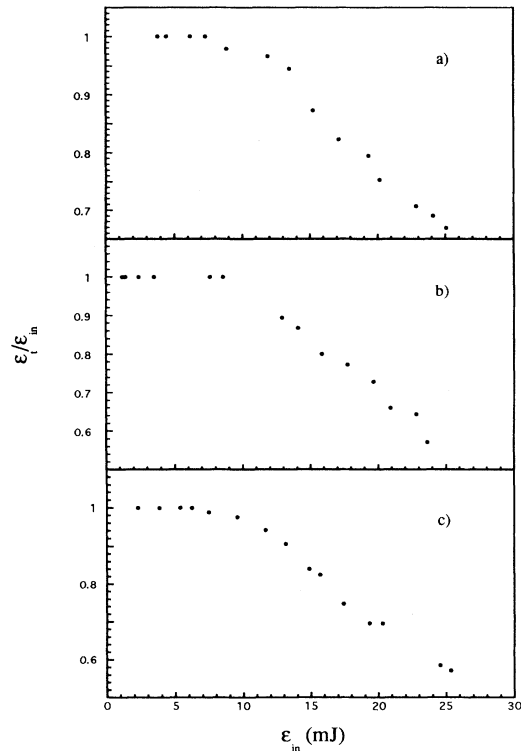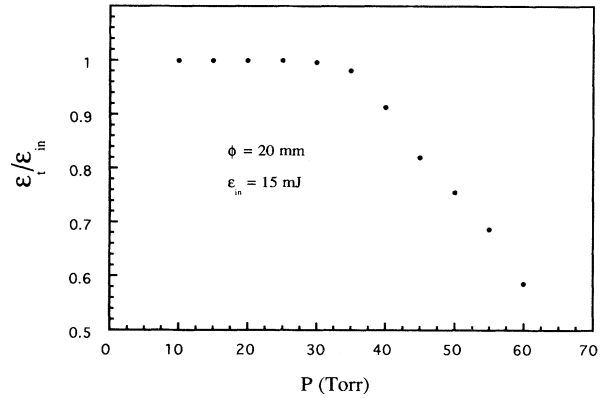

FIG. 11. Energy transmission ratio ϵ_t/ϵ_{in} vs local gas jet pressure P for ϵ_{in} = 15 mJ and diaphragm diameter ϕ=20 mm.

guste *et al.* [7].

As discussed by those authors, one can safely assume that absorption in the plasma is very little, if not absent, and, moreover, the energy required to remove outer shell electrons of noble gas atoms (argon, for instance) in the interaction volume is completely negligible. As a consequence, the reduction in the output laser intensity can only be ascribed to the ionized gas medium, which acts as a diverging lens. In fact, the free-electron density builds up faster on the laser axis, i.e., at the peak of the Gaussian radial intensity profile. This mechanism, which is a strongly nonlinear function of the laser intensity, leads to a radial electron density profile much steeper than the laser intensity profile. As a result, the refractive index of the gas is a minimum on the laser beam axis and the ionized gas acts as a diverging lens. This is exactly the same process that causes defocusing of the third-harmonic beam, although the effect is reduced because of the scaling law of the refractive index with the inverse square of the radiation frequency. The output beam becomes larger than the diaphragm dimension and only a fraction of the output beam can be collected by the joule meter.

Our results fully confirm the data of Ref. [7], but at much lower laser intensities. They also confirm that the problem of choosing the optimum conditions when using harmonic generation in gases as a source of coherent, short-pulse vuv radiation in a given application is still an open one.

B. Scattering cross section

In order to test the analytical model presented in Secs. II and III, we have measured the cross section σ for the scattering of the fundamental beam by the electron plasma. Referring to the definition (37) of σ, we have measured the scattered energy ϵ_{sc} by detecting the laser beam energy emerging from a circular beam stop placed on the beam axis and downstream the interaction region. The beam stop diameter is chosen in such a way as to avoid that the unperturbed beam energy can reach the

FIG. 10. Energy transmission ratio ϵ_t/ϵ_{in} vs laser pulse energy ϵ_{in} in argon (local pressure 40 Torr) for three diaphragm diameters (a) ϕ =3 mm, (b) ϕ=10 mm, and (c) ϕ =20 mm.

detector.

Figure 12 shows the transmission scattering cross section $\sigma_t/\pi w_0^2 = \epsilon_{sc}/\epsilon_{in}$ [see Eq. (39)] as a function of the gas pressure P in the interaction volume at fixed laser intensity. We observe two distinct regions: at low pressures, $\epsilon_{sc}/\epsilon_{in}$ is almost 0 and does not depend on P, as a consequence of the fact that the input beam is basically unperturbed and its transverse dimension remains smaller than the beam stop diameter. This is exactly the case for an obstacle diameter of 10 mm (triangles), whereas for an 8 mm diameter (diamonds) a small amount of energy is still detected. This circumstance shows that the unperturbed beam diameter at the obstacle position is roughly 9 − 10 mm. For pressures above 6 atm a considerable fraction of the incident power is scattered off axis and emerges from the obstacle. In this region, experimental points are suitably fitted by a quadratic curve [see Eq. (39)].

C. Divergence of the third harmonic

The dependence of the third-harmonic photon number N_{ph} produced in argon on the laser pulse energy ϵ_{in} is shown in Fig. 13 in a log-log plot. The experimental points represent averages of 100 laser shots with a local gas pressure of about 40 Torr. As is well known [20], one observes two distinct regions: the low energy region ($\epsilon_{in} \leq 20$ mJ, in our case) is characterized by a slope of about 3, which is in good agreement with the power low $N_{ph} \propto \epsilon_{in}^q$, $q = 3$ being the order of nonlinearity of the process. For $\epsilon_{in} \geq 20$ mJ the slope changes rather abruptly, becoming smaller than 3 ($\simeq 1.5$). This is mainly due to saturation of multiphoton ionization in the gas medium, which takes place in argon at a laser intensity of about 3×10^{13} W cm^{-2}. In this case the
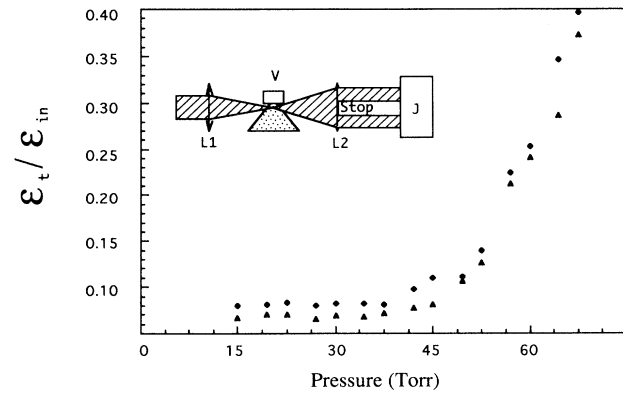

FIG. 13. Third-harmonic photon number N_3 vs laser intensity I, measured in an Ar gas jet at 40 Torr.

ionization probability is almost unity and the nonlinear medium consists of argon ions whose third-order nonlinear susceptibility is reported to be much smaller (10 − 20 times) than that of the neutral atom [1].

In the same experimental conditions, similar results have been reported in xenon, although the saturation intensity is considerably smaller in this case ($\simeq 1 \times 10^{13}$ W cm^{-2}) and corresponds to a laser pulse energy of about 6 mJ. However, the conversion efficiency in xenon is almost 30 times larger than that of argon.

To test the predictions of the model illustrated in Sec. IV, we have used the experimental setup of Fig. 9 to measure the divergence of the third-harmonic beam generated in argon at different laser intensities and gas pressures, namely, as a function of the degree of ionization in the interaction volume. The harmonic beam divergence is, in fact, expected to increase monotonically with the electron density in the focal region.

We report in Fig. 14 the third-harmonic beam divergence angle θ_3 in argon as a function of the laser pulse energy, in the case of argon with a local pressure of about 40 Torr. Each experimental point corresponds to an average over 100 laser shots. Given the elliptical spatial profile of the intensity distribution of the generated vuv radiation, the divergence angle has been detertmined by measuring both the major and the minor axis of the elliptical section at $1/e^2$ of the maximum intensity at various distances from the Rowland circle of the grating, i.e., from the exit slit of the monochromator. Since we have observed the same behavior in both cases, only the values corresponding to the major axis are reported.

The data of Fig. 14 refer to a CCD detector placed 30 cm far from the exit slit. Similar measurements have been carried out at different distances (25 and 40 cm, e.g.) in order to rule out near-field diffraction effects and the trend of Fig. 14 has been confirmed.

FIG. 12. Energy transmission ratio ϵ_t/ϵ_{in} vs local gas jet pressure P for two stop diameters $\phi = 8$ mm ($\triangle$) and 10 mm ($\Diamond$). The apparatus used for measuring the scattered energy is illustrated in the inset. The Nd:YAG laser is focused through the lens L_1 ($f = 25$ cm) to the center of the atomic jet produced by the pulsed valve V. The exit beam is imaged on the joule meter J by means of the lens L_2 ($f = 15$ cm). The central spot is intercepted by a stop having diameters $\phi = 8$ and 10 mm.
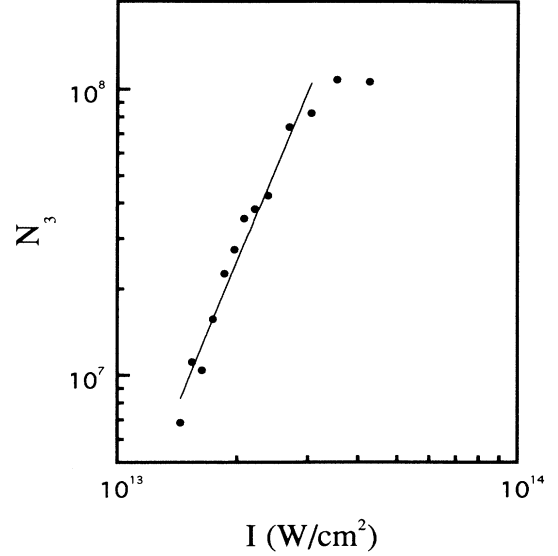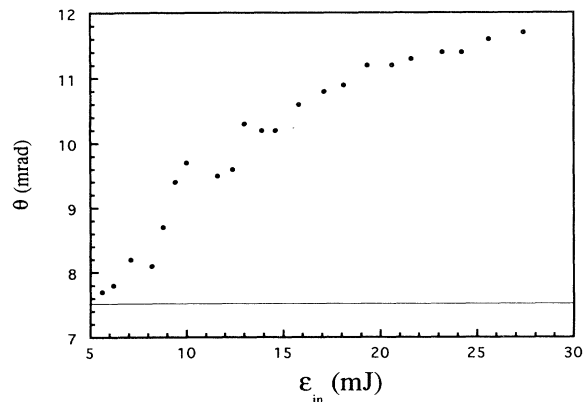
FIG. 14.   Third-harmonic divergence θ in argon as a function of the laser pulse energy ϵ_{in} (mJ). The horizontal line corresponds to the lowest-order perturbation theory prediction.

The increase in the third-harmonic beam divergence is clear and it comes out to be larger than 50% for laser energies of the order of 25 mJ. As already observed, in our conditions this energy corresponds to the saturation of multiphoton ionization of argon. At higher laser intensities, the effect seems to saturate. This behavior can be interpreted as due to the saturation of the ionization and thus to the leveling of refractive index inhomogeneities along the transverse direction in the gas medium.

At lower pulse energies (below 10 mJ), with corresponding lower electron densities in the gas, θ_3 approaches the limit predicted by the lowest-order perturbation theory, namely $\theta_3 = \theta_1/\sqrt{3} \simeq 7.5$ mrad, where $\theta_1 \simeq 13$ mrad is the fundamental laser beam divergence. This confirms that a perturbative approach to the problem is only applicable in case of low order harmonics (third and fifth, particularly) and moderate laser intensities (below 10^{13} W cm^{-2}).

We have also investigated the dependence of the defocusing effect on the density of free electrons in the laser-plasma interaction volume by changing the local gas pressure at fixed laser pulse energy. By increasing the gas target pressure from 30 to 70 Torr, the value of θ_3 increases steadily according to an almost linear low. The effect is not as dramatic as the one shown in Fig. 14. Nonetheless, it is noticeable, with a maximum increase of the order of 25% at the highest investigated pressure ($\simeq 70$ Torr). Moreover, we do not observe saturation effects and the third-harmonic beam divergence keeps increasing with the local gas pressure, at least in the investigated pressure range. We were not able to measure θ_3 at higher local pressures because of pumping speed problems of our vacuum system.

In concluding this section, it is worth stressing that we have also carried out the same measurements in xenon. For the sake of brevity, we do not report here a full description of the xenon data and limit ourselves to point out that we have observed very similar results. The defocusing effect of the laser fundamental and third-harmonic beams brought about by the interaction with the plasma

are very clear and even more dramatic than in argon. Due to the lower ionization potential of xenon and the corresponding lower saturation intensity ($\simeq 1.3 \times 10^{13}$ W cm^{-2}), the increase in the third-harmonic beam divergence starts at lower laser pulse energies ($\simeq$5 mJ) and is so large that in some experimental circumstances the grating of our monochromator (diameter $\varphi = 63$ mm) cannot intercept the whole cross section of the harmonic beam.

We are presently making an effort to analyze the behavior of the fifth-harmonic beam in both gases. The main problem lies in the very low quantum efficiency of the CCD detector that makes it very difficult to obtain precise and reliable data.

VII. CONCLUSIONS

We have discussed the effects of the propagation through an electron plasma of the pump and harmonic beams in harmonic-generation experiments. In particular, we have focused the attention on an incident TEM$_{00}$ Gaussian beam, although our model can be extended without modifications to the case of higher-order Gaussian beams by simply redefining the initial components $E_1^{(m)}$ of the vector $\mathbf{E}_1$ [see Eq. (42)] formed by the amplitudes of the Gauss-Laguerre modes used for expanding the fundamental and the harmonics.

We have also shown that simple approximate expressions of the scattered fundamental field and of the harmonics can be obtained by expanding the fields in power series in the parameter $\Delta\phi$, which measure the effective dephasing undergone by the incident beam in passing through the plasma. As a result of several computations the fields can be approximated by $\mathcal{E} = \mathcal{E}^0 + \Delta\phi\mathcal{E}^1$ for $\Delta\phi$ less than 10.

An effective scattering cross section σ has been introduced for describing the interaction of the incident beam with the plasma. An analytic expression of σ as a function of the saturation parameter s and neutral atom density $\mathcal{N}_{\max}$ has been derived for the case of single scattering (Born approximation).

On the other hand, expanding the scattered field of the fundamental in a power series in the saturation parameter s of the ionization process, we have shown [see Eqs. (63) and (64)] that each term of order k ($=1,2,\ldots$) of this series is well represented by a TEM$_{00}$ mode with divergence θ_k larger than the divergence of the incident beam θ_0 (for a uniform gas density $\theta_1 = 2.26\theta_0, \theta_2 = 2.71\theta_0, \theta_3 = 3\theta_0, \theta_4 = 3.23\theta_0, \theta_5 = 3.4\theta_0$, and $\theta_6 = 3.6\theta_0$). Accordingly, the total far field consists of a central unperturbed region and a large pedestal.

The fraction of energy present in this external region depends on the parameter $\Delta\phi$, i.e., on the neutral atom density [see Eq. (19)], and on the saturation parameter, i.e., on the laser pulse energy. Experimental results confirm such behavior and the agreement with our theoretical analysis is qualitatively good.

We have also addressed the problem of the effects of the plasma on different harmonics. To this end we have expressed the qth harmonic as a combination of to TEM$_{r0}$ Gaussian beams $u_q^{(r)}$. The coefficients $E_{q(\text{out})}^{(r)}$ of this se-

ries in the far field are an extension of the phase-matching integral used in Refs. [1, 3].

$E^{(r)}_{q(\text{out})}$ has been expressed as the volume integral of the product of the modes times the nonlinear polarization induced by the incident laser beam. In particular, we have considered the third harmonic generated by a Nd:YAG laser pulse hitting an argon (or a xenon) gas jet and found that the primary effect of a nonuniform refractive index in the focal region is to broaden the far-field harmonic pattern. Details of the pattern strongly depend on the saturation parameter. Such a broadening is due not only to a direct scattering of the harmonic beam by the electron plasma, but also to the defocusing of the pump beam. The direct process has a weaker effect on the harmonics than on the fundamental beam since refractive index inhomogeneities appear *smoother* to shorter wavelengths. The harmonic beam profile does not present a structure like the one observed in the fundamental field. We have also shown that from the measurements of the scattering cross section σ, it is possible, in principle, to gain information on some plasma parameters, such as density and dimensions.

The good qualitative agreement between theoretical predictions and experimental results provides an indirect proof of the validity of the assumption that the electron distribution does not evolve during the laser pulse duration. It can be considered as *frozen* for pulse durations of 30 ps and shorter.

APPENDIX A: MATRIX ELEMENTS $M_1^{(m;n)}$ AND INITIAL VECTOR $\mathbf{E}_{1(\text{in})}$

According to (44) $\mathbf{M}_1$ is given by

$$\mathbf{M}_1 = -\sum_{k=1}^{\infty} \frac{(-s)^k}{k!}\, \mathbf{P}_1^k \cos^{2kp}\psi, \qquad (A1)$$

where $\mathbf{P}_1^k$ stands for the kth power of the matrix

$$\mathbf{P}_1(\Psi; t^*) \equiv \frac{\int_{-\infty}^{t^*} \theta^{2p}(t')\mathbf{I}_1^p dt'}{\int_{-\infty}^{t^*} \theta^{2p}(t')dt'}\cos^{-2p}\psi, \qquad (A2)$$

with $\mathbf{I}_1^p$ the pth power of the intensity matrix $\mathbf{I}_1$ [see (38)]. For a beam u_1

$$u_1 = \cos\Psi \sum_m E_1^{(m)} e^{-(1-i\,\tan\Psi)V/2 - i(1+2m)\Psi} L_m(V) \qquad (A3)$$

$\mathbf{I}_1$ is given by

$$I_1^{(m;n)} = \cos^2\Psi \sum_{r,r'} \tilde{E}_1^{(r)} \tilde{E}_1^{(r')*} C_{mn;rr'}, \qquad (A4)$$

with

$$C_{mn;rr'} \equiv \int_0^{\infty} e^{-2x} L_k(x)L_l(x)L_m(x)L_n(x)dx. \qquad (A5)$$

For u_1 coincident with the TEM$_{00}$ Gaussian mode u_{in} of Eq. (9) and $B = b$,

$$P_1^{k(m;n)}(\psi) = \int_0^{\infty} e^{-x(1+kp)} L_n(x)L_m(x)dx$$

$$= \binom{m+n}{m} \frac{1}{(1+1/kp)^{m+n}} \frac{1}{kp+1}$$

$$\times F\left(-m, -n; -m-n; 1 - \frac{1}{k^2 p^2}\right), \qquad (A6)$$

where F stands for the hypergeometric function. For an annular beam represented by a superposition of a TEM$_{00}$ and a TEM$_{10}$ mode, $E_{1(\text{in})}^{(0)} = E_{1(\text{in})}^{(1)} = 1/\sqrt{2}$,

$$P_1^{k(m;n)} = \int_0^{\infty} e^{-x(1+kp)} L_n(x)L_m(x)$$

$$\times |1 + (1-x)e^{-i2\psi}|^{2kp}dx. \qquad (A7)$$

For a TEM$_{00}$ Gaussian beam the components of the initial vector $\mathbf{E}_{1(\text{in})}$ read

$$E_{1(\text{in})}^{(m)} = \sqrt{1-a^2}\,a^m, \qquad (A8)$$

with $a = (1 - B/b)/(1 + B/b)$. Finally, for transforming a set of amplitudes $E_1^{(n)}$ relative to modes with $B = b$ to those with $B \neq b$ we can use the matrix of components

$$\int_0^{\infty} e^{-v/2 - V/2} L_m(v)L_n(V)dv$$

$$= (-1)^n \frac{2}{V/v+1} \binom{m+n}{n} \left(\frac{V/v-1}{V/v+1}\right)^{m+n}$$

$$\times F\left[-m, -n; -m-n; \left(\frac{V/v+1}{V/v-1}\right)^2\right]. \qquad (A9)$$

APPENDIX B: MATRIX ELEMENTS $M_q^{(m;n)}$

According to (72), $\mathbf{M}_q$ is given by

$$\mathbf{M}_q = -\sum_{k=1}^{\infty} \frac{(-sq^p)^k}{k!} \mathbf{P}_q^k \cos^{-2kp}\psi, \qquad (B1)$$

where $\mathbf{P}_q^k$ stands for the kth power of the matrix

$$\mathbf{P}_q \equiv \frac{\int_{-\infty}^{t^*} \theta^{2p}(t')\mathbf{I}_q^p dt'}{\int_{-\infty}^{t^*} \theta^{2p}(t')dt'} \cos^{-2p}\psi \qquad (B2)$$

and $\mathbf{I}_q^p$ represents the pth power of $\mathbf{I}_q$

$$I_q^{(m;n)} = q \int_0^{\infty} e^{-qV} L_m(qV)L_n(qV)|u_1|^2 dV$$

$$= q\,\cos^2\Psi \sum_{r,r'} \tilde{E}_1^{(r)} \tilde{E}_1^{(r')*} C_{mn;rr'}, \qquad (B3)$$

with

$$C_{mn;rr'} = \int_0^{\infty} e^{-(q+1)x} L_m(qx)L_n(qx)L_r(x)L_{r'}(x)dx. \qquad (B4)$$

For u_1 coincident with the TEM$_{00}$ Gaussian mode of Eq. (9) and $B = b$,

$$P_q^{k(m;n)} = q \int_0^\infty e^{-x(q+kp)} L_n(qx) L_m(qx) dx$$

$$= \binom{m+n}{m} \frac{1}{kp/q+1} \frac{1}{(1+q/kp)^{m+n}}$$

$$\times F\left(-m, -n; -m-n; 1 - \frac{q^2}{k^2 p^2}\right). \quad \text{(B5)}$$

APPENDIX C: EQUATION OF MOTION OF F_q AND INTEGRAL EXPRESSION OF $E_{q(\text{out})}^{(n)}$

Plugging the right-hand side of (86) into (66) yields

$$\sum_r U_q^{(r)} \frac{dF_q^{(r)}}{d\Psi} = i \cos^{-2} \Psi \frac{\mathcal{P}_q}{\mathcal{P}_{q(\max)}}. \quad \text{(C1)}$$

Next, multiplying (C1) by $U_q^{(r)*}$ and integrating over the cross section

$$\frac{dF_q^{(r)}}{d\Psi} = i\pi W_0^2 \cos^{-4} \Psi \int_0^\infty U_q^{(r)*} \frac{\mathcal{P}_q}{\mathcal{P}_{q(\max)}} dV. \quad \text{(C2)}$$

Consequently,

$$E_{q(\text{out})}^{(r)} = F_{q(\text{out})}^{(r)} = i\pi W_0^2 \int_{-\pi/2}^{\pi/2} d\Psi \, \cos^{-4} \psi$$

$$\times \int_0^\infty U_q^{(r)*} \frac{\mathcal{P}_q}{\mathcal{P}_{q(\max)}} dV$$

$$= \int_{-\pi/2}^{\pi/2} \frac{\mathcal{N}(\Psi)}{\mathcal{N}_{\max}} g_q^{(r)} \cos^{q-3} \Psi d\Psi, \quad \text{(C3)}$$

where

$$g_q^{(r)}(\Psi) = \cos^{-q-1} \Psi \int_0^\infty \left(1 - f_e + \frac{\chi_{\text{ion}}^{(q)}}{\chi_{\text{at}}^{(q)}} f_e\right)$$

$$\times U_q^{(r)*}(\Psi, V)[u_1(\Psi, V)]^q dV. \quad \text{(C4)}$$

For $q=3$,

$$g_3^{(r)} = \sum_{i,j,k;l} \left[C_{ijk;l} + \left(\frac{\chi_{\text{ion}}^{(3)}}{\chi_{\text{at}}^{(3)}} - 1\right) \right.$$

$$\times \left. \sum_{k=1}^\infty \frac{(-s)^k}{k!} \cos^{2pk} \Psi C_{ijk;l} \right]$$

$$\times \tilde{E}_1^{(i)} \tilde{E}_1^{(j)} \tilde{E}_1^{(k)} \tilde{E}_3^{(r;l)*}, \quad \text{(C5)}$$

with

$$C_{ijk;l} = \int_0^\infty e^{-x(3+kp)} L_i(x) L_j(x) L_k(x) L_l(3x) dx, \quad \text{(C6)}$$

while

$$E_{3(\text{out})}^{(r)} = \int_{-\pi/2}^{\pi/2} \frac{\mathcal{N}(\Psi)}{\mathcal{N}_{\max}} g_3^{(r)}(\Psi) d\Psi. \quad \text{(C7)}$$

APPENDIX D: VECTOR $E_q^{1(k)}$

Expanding the mode amplitudes of (78) in the power series (79) and using the expression (B5) for $P_q^{k(m;n)}$ yields

$$i \frac{d}{d\psi} E_q^{1(k)(n)} = \frac{1}{kp/q+1} \frac{1}{(1+q/kp)^n} \sum_l N_l \cos^{2(kp+l-1)} \psi e^{2in\psi} E_q^{0(0)}$$

$$- \sum_{lm} N_l \frac{(q-1)^{m-n}}{q^m} \binom{m}{n} \cos^{2l+q-3} \psi e^{i(2n-2m-q+1)\psi} E_1^{1(k)(m)}. \quad \text{(D1)}$$

Then plugging the right-hand sides of (77) and (58) into (D1) yields

$$i E_q^{1(k)(n)} = \frac{1}{kp/q+1} \frac{1}{(1+q/kp)^n}$$

$$\times \sum_l N_l \left[\sum_{l',\mu}' N_{l'} c\left(l' + \frac{q-3}{2}, \mu\right) \right.$$

$$\times \int_{-\pi/2}^\psi \cos^{2(kp+l-1)} x \frac{e^{i(2\mu+2n-q+1)x} - (-1)^{\mu - \frac{q-1}{2}} e^{i2nx}}{2\mu - q + 1} dx$$

$$+ i \sum_{l'} N_{l'} c\left(l' + \frac{q-3}{2}, \frac{q-1}{2}\right) \int_{-\pi/2}^\psi \cos^{2(kp+l-1)} x e^{i2nx} (x + \pi/2) dx \right]$$

$$+ \frac{1}{1+kp} \frac{1}{(q+q/kp)^n} \sum_{l,m} N_l \binom{m}{n} \left(\frac{q-1}{q+q/kp}\right)^{m-n}$$

$$\times \left(\sum_{l',\mu} N_{l'} c(kp + l' - 1, \mu) \int_{-\pi/2}^\psi \cos^{2l+q-3} x e^{i(2n-2m-q+1)x} \frac{e^{i2(m-\mu)x} - (-1)^{2m-2\mu}}{m - \mu} dx \right.$$

$$+ i \sum_{l'} N_{l'} c(kp + l' - 1, m) \int_{-pi/2}^{\pi/2} \cos^{2l+q-3} x e^{i(2n-2m-q+1)x} (x + \pi/2) dx \right). \quad \text{(D2)}$$

Consequently,

$$
i\frac{2}{\pi}E_{q(\text{out})}^{1(k)(n)} = \frac{1}{kp/q+1}\frac{1}{(1+q/kp)^n}
$$

$$
\times \sum_l N_l \left[\sum_{l',\mu}{}' N_{l'} c\left(l'+\frac{q-3}{2},\mu\right) \frac{c(kp+l-1,\mu+n-\frac{q-1}{2}) - (-1)^{\mu-\frac{q-1}{2}} c(kp+l-1,n)}{\mu-\frac{q-1}{2}} \right.
$$

$$
\left. + \sum_{l'} N_{l'} c\left(l'+\frac{q-3}{2},\frac{q-1}{2}\right)\left(\sum_\mu{}'\frac{(-1)^{n-\mu}}{n-\mu}c(kp+l-1,\mu) + i\pi c(kp+l-1,n)\right)\right]
$$

$$
+ \frac{1}{kp+1}\frac{1}{(q+q/kp)^n}\sum_{l,m} N_l \binom{m}{n}\left(\frac{q-1}{q+q/kp}\right)^{m-n}
$$

$$
\times \left\{ \sum_{l',\mu}{}' N_{l'} c(kp+l'-1,\mu) \frac{c(l+\frac{q-3}{2},\mu-n+\frac{q-1}{2}) - (-1)^{m-\mu}c(l+\frac{q-3}{2},m-n+\frac{q-1}{2})}{m-\mu} \right.
$$

$$
+ \sum_{l'} N_{l'} c(kp+l'-1,m)
$$

$$
\left. \times \left[\sum_\mu{}' \frac{(-1)^{m-n+\frac{q-1}{2}-\mu}}{m-n+\frac{q-1}{2}-\mu}c\left(l+\frac{q-3}{2},\mu\right) + i\pi c\left(l+\frac{q-3}{2},m-n+\frac{q-1}{2}\right)\right]\right\} \tag{D3}
$$

the sums $\sum_\mu'$ being extended to positive and negative integer values of μ except for terms containing vanishing denominators.

APPENDIX E: BEAMWIDTH

The irradiance distribution may be characterized by the set of moments of u_q,

$$
M_r = q\int_0^\infty |u_q|^2 (qv)^{r/2}dv
$$

$$
= \frac{\sum_{m,n}(-1)^{m+n}E_{q(\text{out})}^{(m)*}E_{q(\text{out})}^{(n)}I_{mn}^r}{\sum_m |E_{q(\text{out})}^{(m)}|^2}, \tag{E1}
$$

where

$$
I_{mn}^r = q\int_0^\infty L_m(qv)L_n(qv)\, e^{-qv}(qv)^{r/2}dv
$$

$$
= \sum_{s=0}^m \sum_{t=0}^n (-1)^{s+t}\binom{m}{s}\binom{n}{t}\frac{\Gamma(s+t+1+r/2)}{s!t!}. \tag{E2}
$$

In particular, the ratio θ^2/θ_0^2 between the effective beamwidth θ and θ_0 (relative to a TEM$_{00}$ mode) is given by

$$
\frac{\theta^2}{\theta_0^2} = \frac{\sum_{m,n}(-1)^{m+n}E_{q(\text{out})}^{(m)*}E_{q(\text{out})}^{(n)}I_{mn}^2}{\sum_m |E_{q(\text{out})}^{(m)}|^2}
$$

$$
= \frac{\sum_n\left[(n+1)E_{q(\text{out})}^{(n+1)*}E_{q(\text{out})}^{(n)} + (2n+1)E_{q(\text{out})}^{(n)*}E_{q(\text{out})}^{(n)} + (n+1)E_{q(\text{out})}^{(n)*}E_{q(\text{out})}^{(n+1)}\right]}{\sum_m |E_{q(\text{out})}^{(m)}|^2}. \tag{E3}
$$

[1] A. L'Huillier, X.F. Li, and L.A. Lompré, J. Opt. Soc. Am. B **7**, 527 (1990).

[2] A. Lago, G. Hilbert, and R. Wallenstein, Phys. Rev. A **36**, 3287 (1987).

[3] A. L'Huillier, L.A. Lompré, G. Mainfray, and C. Manus, Adv. At. Mol. Opt. Phys. Suppl. 1, 139 (1991).

[4] A. L'Huillier, K.J. Schafer, and K.C. Kulander, Phys. Rev. Lett. **66**, 2200 (1991); J. Phys. B **24**, 3315 (1991).

[5] L.A. Lompré, M. Ferray, A. L'Huillier, X.F. Li, and G. Mainfray, J. Appl. Phys. **63**, 1791 (1988).

[6] M.H.R. Hutchinson, M. Faldon, J.P. Marangos, J.P. Muffett, R.A. Smith, J.W.D. Tisch, and C.G. Wahlström, J. Opt. Soc. Am. B **9**, 2094 (1992).

[7] T. Auguste, P. Monot, L.A. Lompré, G. Mainfray, and C. Manus, Opt. Commun. **89**, 145 (1992).

[8] S.C. Rae and K. Burnett, Phys. Rev. A **46**, 1084 (1992); K. Burnett, V.C. Reed, and P.L. Knight, J. Phys. B **26**, 561 (1993).

[9] C. Altucci, N.A. Ansari, R. Bruzzese, C. de Lisio, S. Solimeno, and R.B. Kay, J. Phys. B **26**, 1761 (1993).

[10] L.D. Waynshteyn, *Open Resonators and Open Waveguides* (Golem, Boulder, 1969).

[11] M.R. Sogard, J. Opt. Soc. Am. B **5**, 1980 (1980).

[12] C. Altucci, R. Bruzzese, C. de Lisio, and S. Solimeno,

[13] I.S. Gradsteyn and I.M. Ryzhik, *Table of Integrals, Series and Products* (Academic, New York, 1965).

[14] G.C. Bjorklund, IEEE J. Quantum Electron. **QE-11**, 287 (1975).

[15] R.B. Miles and S.E. Harris, IEEE J. Quantum Electron. **QE-9**, 470 (1973).

[16] J.F. Ward and G.H.C. New, Phys. Rev. A **185**, 57 (1969).

[17] G.W. Faris and H.M. Hertz, Appl. Opt. **28**, 4662 (1989).

[18] L.A. Lompré, A. L'Huillier, M. Ferray, P. Monot, G. Mainfray, and C. Manus, J. Opt. Soc. Am. B **7**, 757 (1990).

[19] C.G. Wahlström, Phys. Scr. **49**, 201 (1994).

[20] X.F. Li, A. L'Huillier, M. Ferray, L.A. Lompré, and G. Mainfray, Phys. Rev. A **39**, 5751 (1989).

Phys. Rev. E **49**, 3316 (1994).